Biological optimization of proton therapy based on repeated PET imaging

Anne Marthe Nassar Lindstad

Master thesis in Medical Physics

Department of Physics and Technology

University of Bergen

June 2024

Supervisors: Kristian Smeland Ytre-Hauge, Helge Henjum and Kathrine Røe Redalen

Acknowledgements

I would like to thank my supervisors prof. Kristian Smeland Ytre-Hauge, postdoc Helge Henjum and prof. Kathrine Røe Redalen. Thank you for giving me the opportunity to dive into the field of proton therapy and hypoxia. I appreciate all the help and feedback throughout this work. I feel privileged to have supervisors that are truly interested and invested in the research. I would also like to thank PhD candidate Guillermo Garrido-Hernandez for help and guidance regarding the HNC patient plans. Lastly, I want to thank my husband and family for your invaluable support. Thank you for encouraging me to work hard to achieve my goals, be curious and to pursue my scientific passion.

Bergen, June 2023

Anne Marthe Nassar Lindstad

Abstract

Background and aim: Proton therapy has the potential to deliver dose in a more precise way than traditional photon therapy, which allows for increased sparing of organs at risk (OAR). The aim of this thesis is to determine the potential to increase the biological dose to the biologic target volume (BTV) through biological optimization using proton therapy in the most precise and effective way and simultaneously spare the OARs, as well as to explore the use of imaging to adapt target dose and to ensure tumor control, through testing and exploring an optimization tool developed at the University of Bergen.

Material and methods: Intensity modulated proton therapy treatment plans for a water phantom and head and neck cancer (HNC) patients were created in Eclipse Treatment Planning System. The plans were optimized in a FLUKA based optimization tool developed at the University of Bergen. The water phantom was linear energy transfer (LET) optimized, and the BTV was subject to a 1.1 relative biological effectiveness (RBE) weighted dose escalation as well as LET escalation, while the dose and LET of the OAR was minimized. Furthermore, a method for RBE and oxygen enhancement ratio (OER) weighted dose optimization was implemented in the optimization tool. Subsequently, the water phantom was RBE and OER weighted dose (ROWD) optimized to achieve a homogeneous ROWD over the clinical target volume and the BTV. The ROWD optimization was performed with different values of oxygen pressure level of the BTV to investigate the effect of hypoxia with the optimization tool. Various optimization strategies were investigated, and the most promising ROWD optimization strategies were applied on 5 HNC patient plans.

Results: The dose-averaged LET (LET_d) of the BTV increased and the LET_d of the OAR decreased simultaneously, without significant changes in the dose of the structures when considering LET_d optimization of the water phantom. A homogeneous ROWD of the BTVs was achieved successfully for both the water phantom and the patient plans, and the level of oxygen in the BTVs did not have a noteworthy effect on the dose or LET_d of the OARs.

Conclusion: The optimization of biological dose with the optimization tool was successful for both LET_d and ROWD optimization. The OARs were successfully spared in the optimizations. The results contribute to the idea of biological optimization being a promising technique in proton therapy which could significantly improve treatment as more precise techniques to quantify pO_2 emerge.

Contents

Abbreviations

BTV	Biologic target volume
CTV	Clinical target volume
DAH	Dahle OER model
DAHANCA	Danish Head and Neck Cancer
D_{bio}	Biological dose
DE	Dose escalation
DE-LET_{BTV}	Dose escalation and LET escalation to BTV
DE-$LET_{BTV, OAR}$	Dose escalation and LET escalation to BTV, LET restriction to OAR
DICOM	Digital Imaging and Communications in Medicine
DPBC	Dose painting by contours
D_{phys}	Physical dose
DVH	Dose volume histogram
GTV	Gross target volume
Gy	Gray
HNC	Head and neck cancer
HU	Hounsfield units
IMPT	Intensity modulated proton therapy
LET	Linear energy transfer
LET_d	Dose averaged-linear energy transfer
LET_Δ	Restricted LET
LET_∞	Unrestricted LET
LVH	LET volume histogram
LQ	Linear-quadratic
MC	Monte Carlo

MRI	Magnetic resonance imaging
OAR	Organ at risk
OER	Oxygen enhancement ratio
PDF	Probability density function
PET	Positron emission tomography
pO_2	Partial oxygen pressure
PTV	Planning target volume
RBE	Relative biological effectiveness
ROI	Region of interest
ROWD	RBE and OER weighted dose
SOBP	Spread out Bragg peak
TPS	Treatment planning system
VMAT	Volumetric modulated arc therapy
WEN	Wenzl and Wilkens OER model
^{18}F-FDG	^{18}F-fluorodeoxyglucose

1. Introduction

Cancer is the most common cause of death in Norway [1]. According to the Cancer Registry of Norway, about 33 % of all Norwegians will develop cancer before the age of 75 years [2]. Cancer can be treated with radiation therapy, chemotherapy, surgery and immunotherapy. Late effects due to the cancer treatment is common among the survivors [3, 4]. Proton therapy has the potential to lower the occurrence of late effects compared to radiation therapy by decreasing the irradiation of healthy tissue [5, 6]. Two proton therapy centers will open in Norway in the near future, which gives new opportunities for cancer treatment in the country.

1.1 Proton therapy and hypoxia

Proton therapy is a cancer treatment technique based on using beams of protons to irradiate the tumor. The idea of using protons for cancer treatment was first proposed by Robert Wilson in 1946 [7]. The depth-dose curve of a proton beam differs from a photon beam, as shown in Figure 1. As opposed to a photon beam, most of the dose of a proton beam is deposited at the end of the path [8]. This gives rise to a peak in the depth-dose curve, called the Bragg peak. Proton therapy offers a more precise dose delivery than traditional radiation therapy by exploiting the Bragg peak, which makes it a preferable treatment technique for treating tumors with many surrounding organs at risk (OARs) [9]. This is typically the case for head and neck cancer (HNC). One challenge in the treatment of HNC is the variation in tumor radiosensitivity across patients and within each tumor. The difference in radiosensitivity often origin from the hypoxic nature of sub-volumes within the tumor. Hypoxic tissue is defined as tissue with low oxygen concentration, which leads to the tissue being more radioresistant [10]. To account for the varying radiosensitivity of the tumor, the concept of dose painting can be applied. Dose painting is a dose delivery technique that allows for inhomogeneous dose distributions in the target, which enables escalation of dose to the more radioresistant sub-volumes within the tumor [11]. The steep dose gradient characteristic for proton therapy makes the escalation in sub-volumes possible.

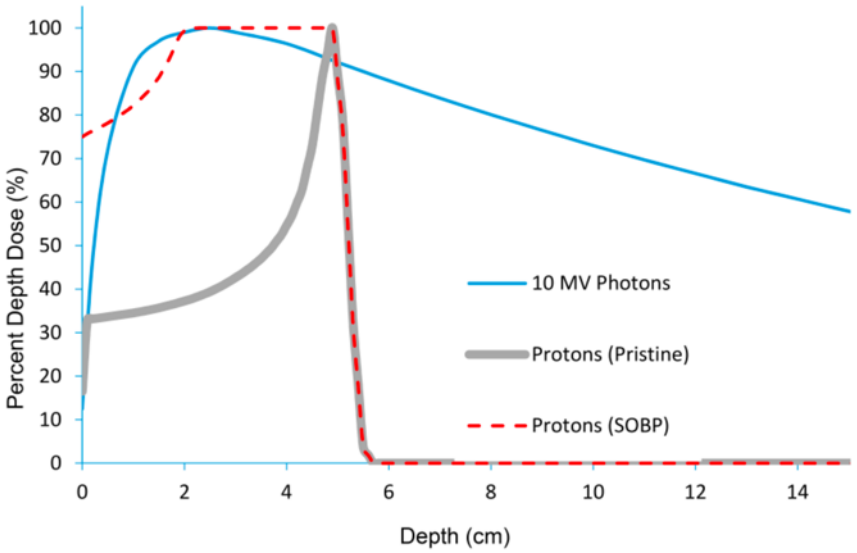

Figure 1: Percent depth dose as a function of depth in water for a photon beam, a pristine proton beam and a spread-out Bragg peak (SOBP). Figure from [12].

Some important concepts in proton therapy are LET and RBE. LET is a quantity defined as the energy transferred to the media through local ionizations per unit length by ionizing radiation [8, 13]. It increases with decreasing velocity of the protons in the proton beam. RBE is defined as the ratio of the reference photon dose to the dose of another ionizing radiation necessary to cause the same level of effect [8]. It is dependent on LET fraction dose, the radiosensitivity parameters α and β as well as other biological and physical factors [14, 15]. For clinical use, the RBE of protons is set to 1.1 by convention. When considering proton therapy of hypoxic tumors, it is important to include the concept of OER. OER is defined as the ratio between the dose at a certain oxygen pressure and the dose at the aerobic oxygen pressure that causes the same level of effect to the cells [8]. RBE and OER weighted dose (ROWD) takes into account both the effectiveness of proton irradiation as well as the radiosensitivity of the hypoxic tissue. Hence, including ROWD in the treatment planning may contribute to a better treatment outcome.

Positron emission tomography (PET) is an imaging modality that can image metabolism and biochemical activity in the tissue, and has the potential of identifying sub-volumes where the biological dose should be escalated [16, 17]. These sub-volumes are often denoted BTVs, and can be identified through biological imaging

[17]. The biological dose can be escalated through escalation of the physical dose and/or LET. Comparing baseline and interim ^{18}F-FDG PET images has been proposed as a way of defining the BTVs in potentially hypoxic tumors [18]. This is a simplified way of identifying hypoxic tissue, and a different radiotracer should be used if the goal is to estimate tumor hypoxia directly.

1.2 Biological optimization

Biological optimization is suggested as a promising method of treatment planning to improve the treatment outcome [19, 20]. Biological optimization through LET optimization and ROWD optimization is generally not available in clinical treatment planning systems. An optimization tool was therefore developed at the University of Bergen to explore the potential of biological optimization. The code of the optimization tool is written in Python and is based on input from FLUKA Monte Carlo (MC) simulations. The optimization tool currently includes features like robust optimization, variable RBE and LET optimization as well as ROWD optimization. The latter was implemented in the optimization tool in the present work.

1.3 Project objectives

The main objective of this thesis is to determine the potential to increase the biological dose to the BTV through biological optimization using proton therapy in the most precise and effective way, and simultaneously spare the OARs, as well as to test and explore the optimization software developed at the University of Bergen. This will be achieved through the following steps:

- Exploration of LET optimization strategies.
- Find an optimization strategy that gives a homogenous ROWD for the whole BTV, as well as minimal OAR dose.

2. Physics of proton therapy

2.1 Interactions of protons in matter

Protons are charged particles with a definite range in matter. The interactions of protons in matter, relevant for proton therapy, are elastic Coulomb interactions, inelastic Coulomb interactions and inelastic nuclear reactions [8, 13, 21]. The interactions are illustrated in Figure 2.

Elastic Coulomb interactions occur when the proton passes through the matter and interacts with the atomic nuclei. The repulsive Coulomb force deflects the trajectory of the proton, but the energy remains unchanged [13, 21]. As the proton is deflected multiple times, the accumulated deflection leads to lateral spreading of the proton beam. The accumulation of the deflection of the protons is called Multiple Coulomb Scattering [13].

Inelastic Coulomb interactions occur when the proton passes through the matter and interacts with atomic electrons. Due to the attractive Coulomb force, the electrons can be excited or ionized[8]. The local ionizations give rise to the linear energy transfer, as described in section 2.3. The proton will lose some energy in each interaction and slows down, but the initial direction is unchanged. Energy loss due to inelastic Coulomb interactions with the atomic electrons is quasi-continuous and is the main reason for energy loss of a proton beam [13]. The energy loss of a proton is described by the Bethe Bloch equation, as defined in section 2.2.

Inelastic nuclear reactions may occur when the energy of the proton is sufficiently high and the distance to the atomic nucleus is short enough. The proton interacts with the atomic nucleus and a nuclear reaction takes place [21]. This reaction can result in secondary particles like protons, neutrons or ions. Inelastic nuclear reactions are dependent on the atomic number of the nucleus, the distance between the proton and the nucleus and the proton energy, so that the proton can overcome the Coulomb barrier of the nucleus [13]. The inelastic nuclear reactions are more rare than Coulomb interactions, but they have a significant effect as a proton is removed from the proton

beam during the reaction [21]. The fluence of the proton beam decreases as protons undergo inelastic nuclear reactions.

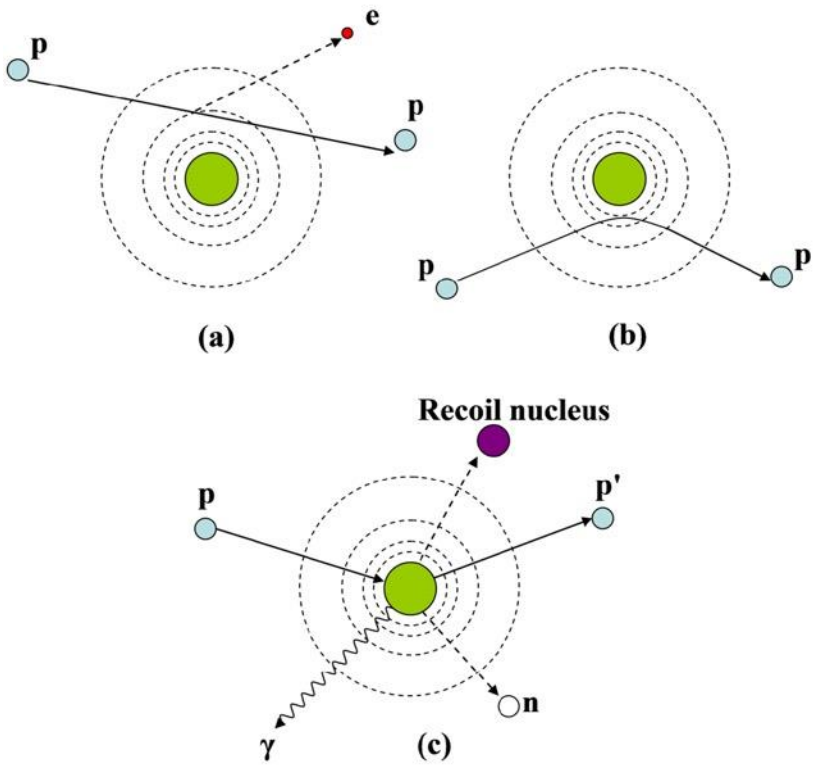

Figure 2: Proton interactions. a) Inelastic Coulomb interaction, b) Elastic Coulomb interaction, c) Inelastic nuclear reaction. Figure from [21].

2.2 Bethe Bloch equation

The energy loss of a charged particle in matter, also called the linear stopping power, is described by the Bethe Bloch equation:

$$-\frac{dE}{dx} = \frac{4\pi N_A r_e^2 m_e c^2 \rho}{\left(\frac{v}{c}\right)^2}\frac{Z}{A}z^2\left(ln\left(\frac{2m_e c^2\left(\frac{v}{c}\right)^2}{I\left(1-\left(\frac{v}{c}\right)^2\right)}\right)-\left(\frac{v}{c}\right)^2\right), \quad (1)$$

where E is the particle energy, x is the distance, N_A is Avogadro's number, r_e is the radius of the electron, m_e is the mass of the electron, c is the speed of light, ρ is the density of the medium, Z is the atomic number of the medium, A is the atomic mass of the medium, z is the charge of the particle, v is the velocity of the particle and I is the

ionization potential of the medium [8, 21]. As seen in the equation, the energy loss increases with decreasing particle velocity.

2.3 Linear energy transfer

Linear energy transfer (LET) is a quantity defined as the energy transferred to the media through local ionizations per unit length by ionizing radiation [8, 13, 22]. LET is usually measured in the unit keV/µm. The quantity depends on the charge and velocity of the particle, as well as the density and atomic number of the medium the particle is traveling through [8]. Restricted LET (LET_Δ) does not include the energy transferred to secondary electrons with energy above Δ, and is given by:

$$LET_\Delta = -\frac{dE_\Delta}{dx}, \tag{2}$$

where dE_Δ is the energy transferred to the media, excluding secondary electrons with energy above Δ, and dx is the distance travelled by the ionizing radiation. Unrestricted LET (LET_∞) includes all energy transferred by the ionizing radiation, and is given by:

$$LET_\infty = -\frac{dE_\infty}{dx}, \tag{3}$$

where dE_∞ is the energy transferred to the media and dx is the distance travelled by the ionizing radiation [23]. Unrestricted LET equals the energy loss as described by the Bethe Bloch in equation (1), and is the quantity that is usually used. Unrestricted LET is also called electronic stopping power, S_{el}. Dose-averaged LET (LET_d) is defined as:

$$LET_d(z) = \frac{\int_0^\infty S_{el}(E)D(E,z)dE}{\int_0^\infty D(E,z)dE}, \tag{4}$$

where D(E,z) is the absorbed dose from a charged primary particle at position z and with kinetic energy E [22]. The LET increases as the velocity of the proton decreases [8]. This results in an increased LET along the particle track, with a maximum LET around the end of the track. The LET also increases with the charge of the particle. Protons used in proton therapy are defined as low LET, while heavier ions such as ^{12}C are defined as high LET [8]. A common way of illustrating LET is through an LET

volume histogram (LVH), which shows LET as a function of volume percentage for a given structure.

2.4 Dose

The essence of radiation and particle therapy is the dose delivery to the tumor. Dose is defined as the energy absorbed by the tissue and is measured in the unit Gray (Gy) [8]. The unit can also be expressed in SI-units:

$$1\ Gy = 1\ J/kg. \tag{5}$$

The depth dose profile of protons in tissue has a characteristic shape. Nearly all the energy is deposited at a certain depth, and this gives rise to the Bragg peak. The depth of a Bragg peak depends on the initial energy of the proton beam. In clinical use, many Bragg peaks are put together to form a spread-out Bragg peak (SOBP) to create a uniform dose in a larger area, as seen in Figure 3 [8]. The absorbed dose, as described in equation (5), is also called physical dose (D_{phys}) [13]. Dose is often illustrated in a dose volume histogram (DVH), which shows the dose as a function of volume percentage of a given structure.

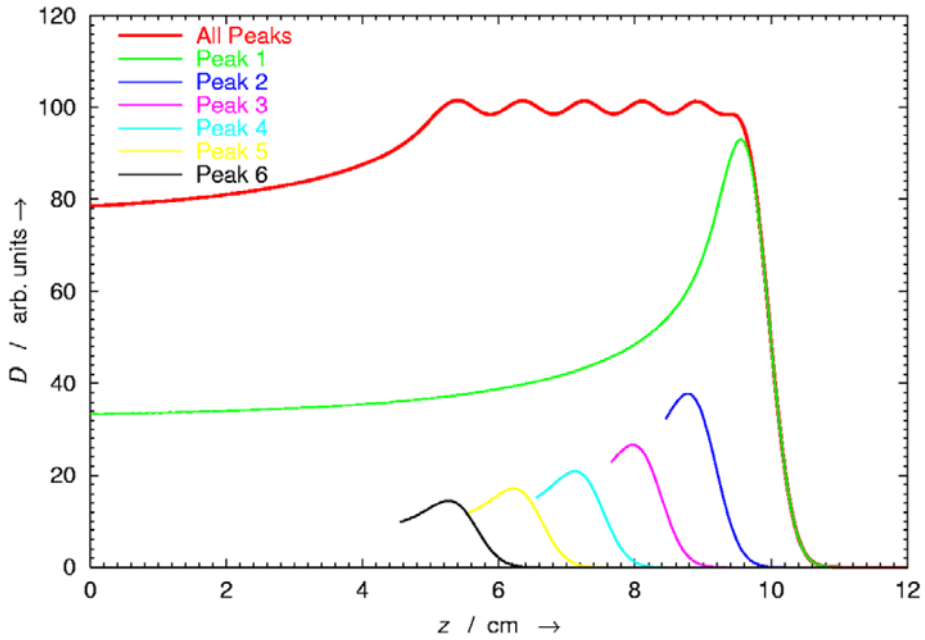

Figure 3: Dose D as a function of depth z in water. A SOBP is shown in red, while the individual Bragg peaks are shown in green, blue, pink, turquoise, yellow and black. Figure from [21].

2.5 Range

Protons have a finite range in matter [8]. The range is not defined for a single proton, but rather as an average quantity for a beam of protons. This is due to the fact that the energy loss varies slightly between the different paths of the protons [21]. This phenomenon is called energy or range straggling. Several definitions of range are applied in the proton therapy community, but most commonly range is defined as the depth where 50 % of the protons have stopped or at the point where the dose is reduced to 80% of the peak dose (R80%) [21]. The latter is easier to determine experimentally. As most of the dose is deposited at the Bragg peak, it is important to know the range of the proton beam to prevent underdosage in the tumor and overdosage in the surrounding healthy tissue. The range of a proton beam in water is illustrated in Figure 4.

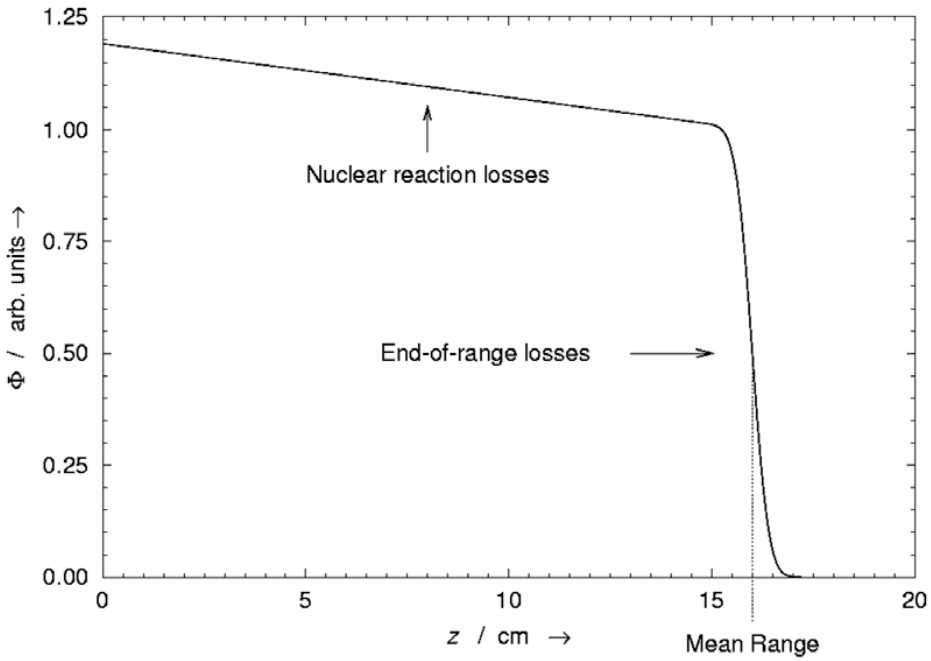

Figure 4: Relative fraction of fluence Φ as a function of depth z in water for a beam of protons. Figure from [21].

3. Radiobiology

Biological damage to the DNA by radiation or particle therapy can be categorized as direct or indirect action. Direct action is defined as direct ionization of the DNA, while indirect action is defined as ionization of water molecules which create free radicals that subsequently can damage the DNA. Indirect action increases with the oxygen level, as opposed to direct action which does not depend on the oxygen level [8]. As low oxygen levels decrease the occurrence of indirect action, hypoxic tumors will be more radioresistant than well-oxygenated tumors [24, 25]. This is further discussed in section 3.5.

Double-strand break of the DNA is the main mechanism leading to cell death by ionizing radiation [8]. It can occur after hits by both a single particle and by multiple particles. A single particle can hit both strands in one hit or cause damage to the bases between the DNA strands by many hits, as shown in Figure 5. Two or more particles can cause damage to the DNA strands, which in turn can lead to double-strand break [8].

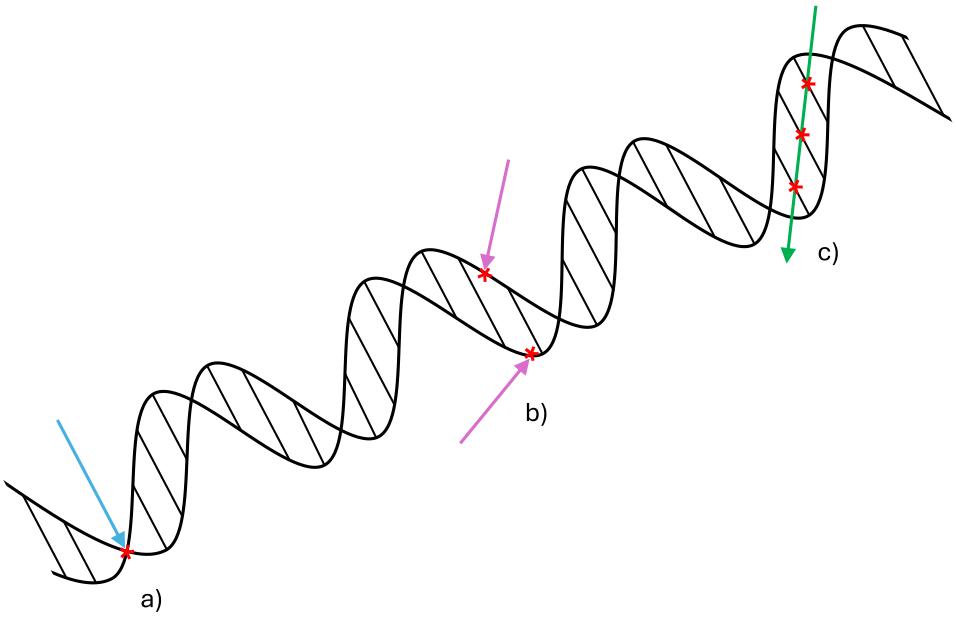

Figure 5: DNA damage caused by ionizing radiation. a) Single hit by one particle, b) Two hits by two particles, c) Multiple hits by one particle.

3.1 Linear-quadratic model

The linear-quadratic model (LQ model) is a model of the survival fraction of cells after ionizing radiation and it considers the different mechanisms of DNA damage [8]. Single-hit kill, denoted by α, is defined as the unrepairable DNA damage. Two-hit kill, denoted by β, is defined as the repairable DNA damage. The parameters α and β are also known as the radiosensitivity parameters. The radiosensitivity parameter α does not depend on fractionation or dose rate, as opposed to β. The α/β ratio is a measure of how tissue is affected by the fraction size and is defined as the dose when the level of α and β kills are equal [8]. Tissues with a low α/β ratio are more resistant for small fraction sizes and more sensitive for large fraction sizes, while the trend is opposite for tissues with a high α/β ratio. A low α/β ratio is around 1-3 Gy and a high α/β ratio is around 10 Gy. Tissues with a low α/β ratio can be characterized as late-reacting, while tissues with a high α/β ratio can be characterized as acute-reacting [8]. The LQ model is given by:

$$SF_D = e^{-(\alpha D + \beta D^2)}, \tag{6}$$

where SF_D is the survival fraction of a given dose D, and α and β are the radiosensitivity parameters [8]. Figure 6 shows the survival fraction as a function of dose.

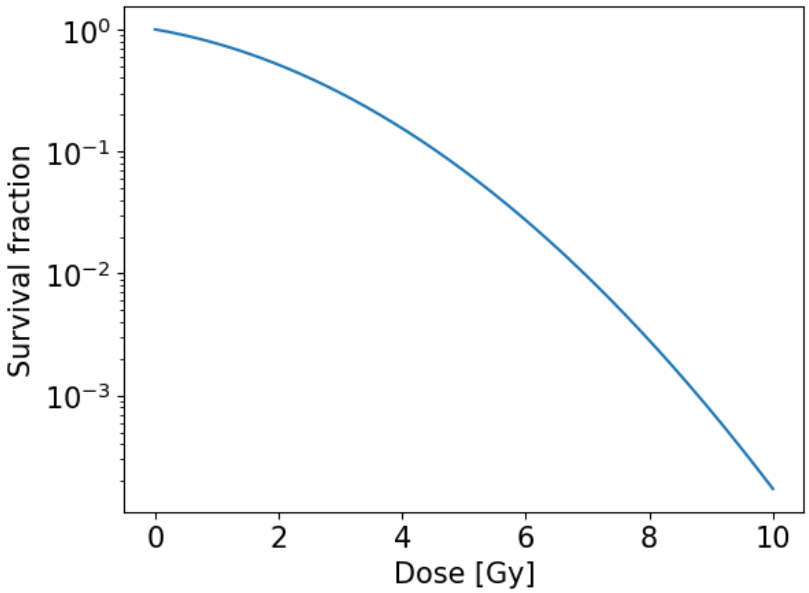

Figure 6: Survival fraction as a function of dose.

3.2 Relative biological effectiveness

Relative biological effectiveness (RBE) is defined as the ratio of the reference photon dose to the dose of another ionizing radiation necessary to cause the same level of effect [8, 26]. It is a unitless quantity that says something about the efficiency of the type of radiation. RBE can be expressed as:

$$RBE = \frac{D_{reference}}{D_{test}}, \tag{7}$$

where $D_{reference}$ is the dose of the reference photon radiation and D_{test} is the dose of the test radiation. The RBE of protons is set to 1.1, based on *in vitro* data [27]. However, many *in vitro* studies show that the RBE is not constant, and that it is highest at the end of the SOBP [14, 15, 27]. The RBE depends on several factors such as LET, fraction dose, α/β ratio and other physiological and biological factors [14, 15]. There are several variable RBE models, some examples are the Lyngholm model, McNamara model, Wilkens model, Wedenberg model and the Carabe model [28-32]. In proton therapy it is common to use RBE-weighted dose, defined by:

$$D_{bio} = D_{phys} \cdot RBE, \tag{8}$$

where D_{bio} is the biological dose and D_{phys} is the physical dose [33].

3.3 Intensity modulated proton therapy

Intensity modulated proton therapy (IMPT) is a treatment delivery technique based on spot scanning with proton pencil beams, as shown in Figure 7 [8]. As specified in the name, the intensity of the proton beam can be modulated over the target. IMPT delivers a three-dimensional dose to the target volume. The shape of each layer in the xy-plane is created by magnets, while range shifters create new layers in the z-direction. IMPT is commonly viewed as the future of proton therapy [13, 34]. Dose-painting is the concept of dose escalation to tumor sub-volumes, usually applied to BTVs [17]. Dose-painting can be performed through dose-painting by numbers or dose-painting by contours (DPBC), which is dose escalation based on voxels or structure contours, respectively [35].

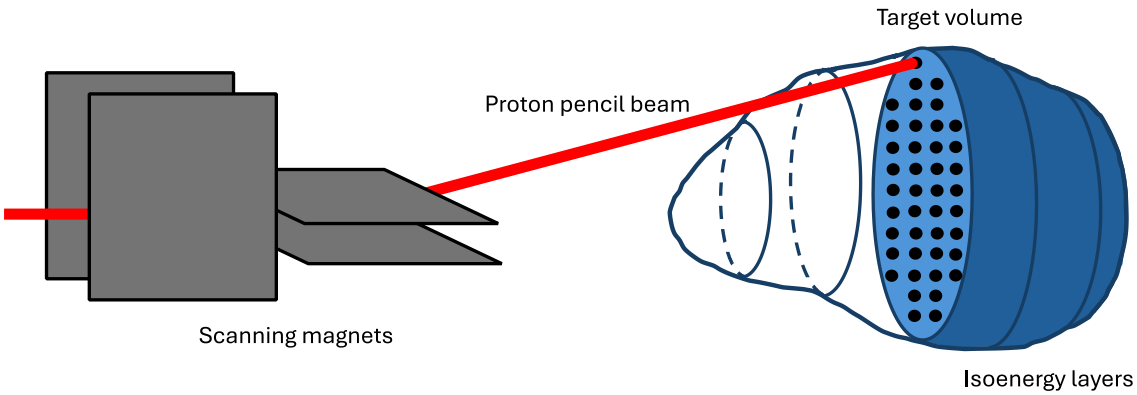

Figure 7: Spot scanning by a proton pencil beam.

3.4 Target volumes

Different kinds of target volumes are used in the process of treatment planning [36-38]. Gross tumor volume (GTV) is defined as the disease that is visible, palpable or seen through imaging. The clinical target volume (CTV) is defined as the GTV and the surrounding tissue that is suspected to contain subclinical disease, thus including a margin around the GTV. Planning target volume (PTV) is defined as the CTV as well as setup margins, to account for geometrical uncertainties [36]. In addition to these target volumes, the biologic target volume (BTV) can be defined from the biological characteristics of the tumor [17]. It can be identified through biological and biochemical imaging techniques, such as PET imaging and magnetic resonance imaging (MRI). These imaging techniques give information of hypoxia, tumor burden and tumor growth. The purpose of including the BTV in the treatment planning is to increase the local-regional control [17, 39]. In radiation therapy it is assumed that as long as the PTV receives the prescribed dose, the CTV will also receive the prescribed dose [34]. Due to range uncertainty and modulation of fields in IMPT, this assumption is not generally correct for IMPT. Hence, robust optimization is introduced to account for the uncertainties [34]. Robust optimization is further discussed in section 4.3. The target volumes are illustrated in Figure 8.

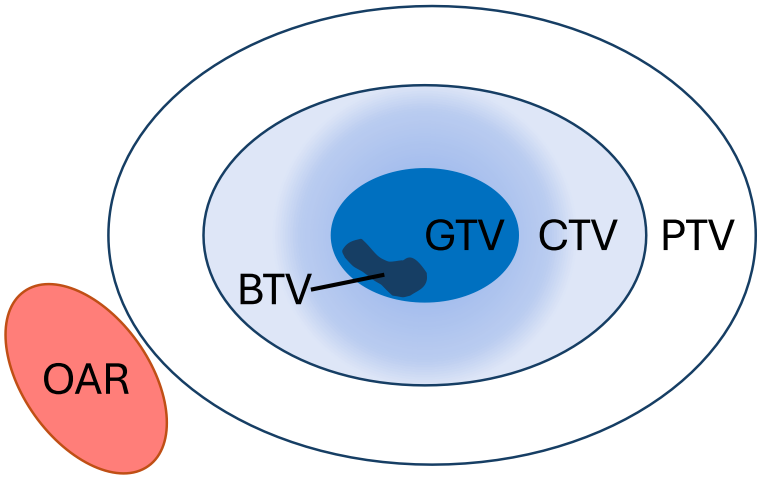

Figure 8: Target volumes GTV, CTV, PTV and BTV with an OAR outside the target volumes. Figure inspired by [37].

3.5 Hypoxia

Hypoxic tissue is defined as tissue with low oxygen partial pressure levels (pO_2), as opposed to normoxic tissue which has normal levels of pO_2. Hypoxia is a result of an imbalance in the consumption and supply of oxygen to the cells [40]. Normoxic pO_2 varies between different kinds of tissue [41]. Hence, there are several values for normoxic and hypoxic pO_2. In general, hypoxic tissue has pO_2 levels below 8-10 mmHg [42]. Hypoxia can also be defined as extreme hypoxia (pO_2 of 0-0.5 mmHg), hypoxia (pO_2 of 0.5-5 mmHg) and moderate hypoxia (pO_2 of 5-20 mmHg), while normoxic pO_2 is defined as above 20 mmHg [43]. The pO_2 of air is 160 mmHg, and this value is usually used as the normoxic pO_2 in *in vitro* studies. Hypoxic regions are often found in locally advanced solid tumors and are more radioresistant than normoxic tissue [24]. Hypoxia can be defined as acute or chronic hypoxia. Acute hypoxia is caused by limited perfusion of O_2 to the tissue, and the condition is often transient. Chronic hypoxia is caused by increased diffusion distances for the O_2, often as a result of tumor expansion. Both acute and chronic hypoxia is caused by inadequate O_2 delivery to the tissue [24, 40]. Measurements of pO_2 can be performed in several ways. Polarographic sensors are considered as the “gold standard” and are based on measuring the voltage difference between polarographic pO_2 electrodes. The disadvantage of the method is the fact that it is invasive [41].

3.5.1 Oxygen enhancement ratio

The oxygen enhancement ratio (OER) is defined as the ratio between the dose at a certain oxygen pressure D_h and the dose at the aerobic oxygen pressure D_a that causes the same level of effect to the cells [8]:

$$OER = \frac{D_h}{D_a}. \tag{9}$$

There are several OER models, among them the Dahle model (DAH), Wenzl and Wilkens (WEN), Mein, Strigari and the Tinganelli model [44-48]. Figure 9 shows the OER models as a function of pO_2. The DAH model is based on the model by Wenzl and Wilkens, which parametrizes the radiosensitivity parameters of the LQ model to account for hypoxia and LET. The model coefficients of the WEN model are based on *in vitro* data from irradiation with several kinds of ions, while the DAH model only uses data from proton irradiation for the model coefficients [44, 45]. The parametrized radiosensitivity parameters of WEN and DAH are given by:

$$\alpha(L,p) = \frac{(a_1 + a_2 \cdot L) \cdot p + (a_3 + a_4 \cdot L) \cdot K}{p + K}, \tag{10}$$

and

$$\sqrt{\beta(p)} = \frac{b_1 \cdot p + b_2 \cdot K}{p + K}, \tag{11}$$

where L is the LET_d, p is the pO_2, K, a_1, a_2, a_3, a_4, b_1 and b_2 are constants specified in Table 1. The DAH and WEN models of OER are given by:

$$OER = \frac{\sqrt{\alpha^2(L,p_h) - 4\beta(p_h) \cdot \ln(S)} - \alpha(L,p_h)}{\sqrt{\alpha^2(L,p_a) - 4\beta(p_a) \cdot \ln(S)} - \alpha(L,p_a)} \cdot \frac{\beta(p_a)}{\beta(p_h)}, \tag{12}$$

where α is given in equation (10), L is the LET_d, p_h is the pO_2 of the hypoxic conditions, β is given in equation (11), S is the survival fraction and p_a is the pO_2 of the normoxic (aerob) conditions [44, 45]. The constants a_1, a_2, a_3, a_4, b_1 and b_2 are obtained from *in*

vitro cell lines. Table 1 specifies the constants used in equations (10), (11) and (12) for the DAH model.

Table 1: Constants of the DAH OER model [44].

Constant	a_1	a_2	a_3	a_4
Value	0.1 Gy^{-1}	0.001 µm/(Gy·keV)	0.01 Gy^{-1}	0.001 µm/(Gy·keV)

Continuation of Table 1.

Constant	b_1	b_2	K	p_a	S
Value	0.765 Gy^{-1}	0.237 Gy^{-1}	3 mmHg	30 mmHg	0.10

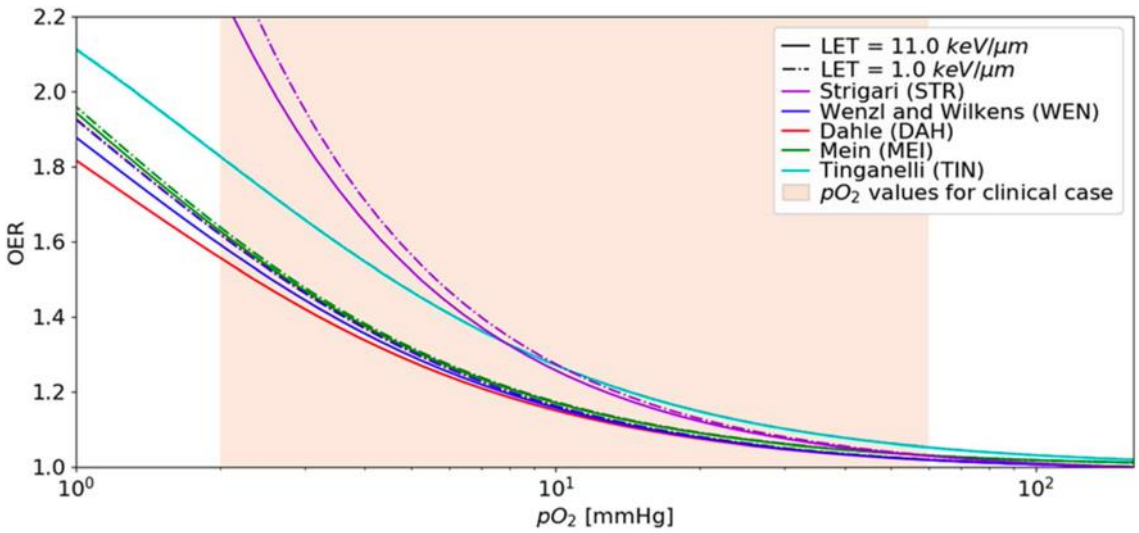

Figure 9: Various OER models as functions of pO_2. Figure from [49].

RBE and OER weighted dose (ROWD) is given by [49]:

$$ROWD = D_{phys} \cdot \frac{RBE}{OER}. \tag{13}$$

It is advantageous to use ROWD when considering hypoxic tissue to account for the lowered radiosensitivity. ROWD has the potential to improve tumor control and

treatment outcome. However, the exact level of pO_2 is rarely known, which results in an uncertainty in the calculation of ROWD.

3.6 Positron emission tomography

Positron emission tomography (PET) is an imaging modality that can image metabolism and biochemical activity in the body [16]. It is based on injecting a radiotracer into the body. The radiotracer decays through β^+ emission. The emitted positron will annihilate with an electron, which results in two photons propagating in opposite directions. The patient is placed on a patient table, surrounded by a detector, as shown in Figure 10. The detector contains scintillation crystals which detects the photons that are emitted. The point of annihilation can be reconstructed, and an image of where the positrons were emitted can be created [16]. There are several radioactive tracers which serve different purposes. The most used radiotracer is ^{18}F-fluorodeoxyglucose (^{18}F-FDG). As tumors often have a high metabolism and glucose consumption, the tumor will normally have a high uptake of ^{18}F-FDG and it can be identified in the image [16]. ^{18}F-FDG does not image hypoxia directly. PET can image tumors and metastases that are not visible on CT images and allows for detection of hypoxia inside the tumor and is a non-invasive three-dimensional imaging technique [10]. Radiotracers for detection of tumor hypoxia should inhabit several characteristics. Some characteristics include specificity to hypoxic cells only, easy to synthesize and no dependence on pH or blood flow. ^{18}F-labelled nitroimidazoles and Cu-labelled diacetyl-bis(N4-methylthiosemicarbazone) analogues are the most common classes of radiotracers for imaging of hypoxia. The most clinically studied radiotracer for hypoxia is ^{18}F-fluoromisonidazole (^{18}F-FMISO), which can be used to detect hypoxia in several kinds of tumors [10]. ^{18}F-MISO is however not ideal for all tumors and has limited contrast. Another radiotracer used for hypoxia detection is ^{18}F-labelled 2-(2-nitro-1H-imidazol-1-yl)-N-(2,2,3,3,3-pentafluoropropyl)-acetamide (^{18}F-EF5) [50].

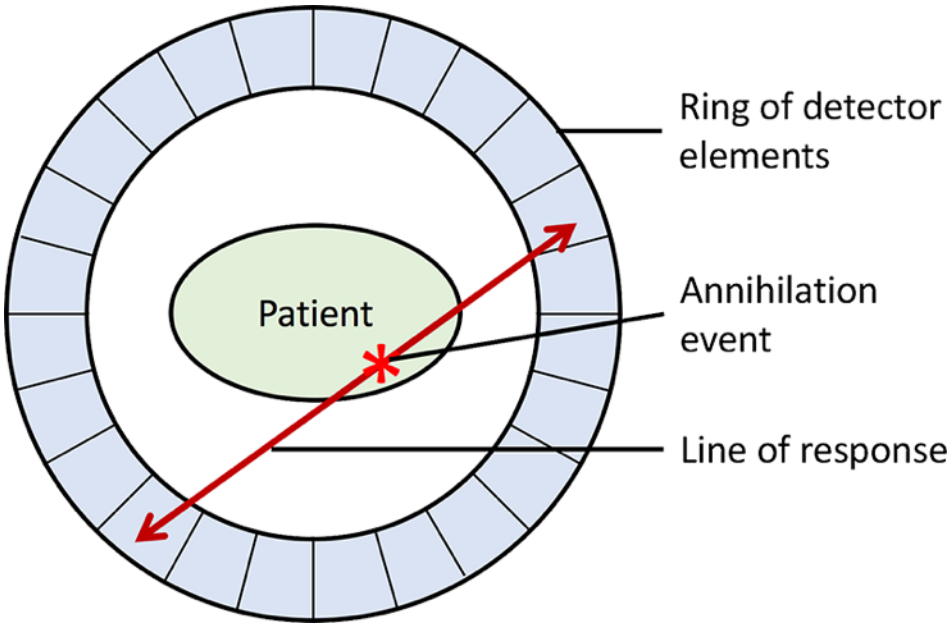

Figure 10: Sketch of a PET detector with a patient inside. Figure from [51].

4. Monte Carlo simulations and Treatment optimization

4.1 The Monte Carlo method

The Monte Carlo (MC) method is a method for modelling stochastic processes [52, 53]. It is considered as the most precise way of calculating dose in radiation and particle therapy [54]. The method is based on random sampling of probability density functions (PDFs) that model a system. The PDFs define the space of possibilities and the relative possibilities for a given event. MC simulations allow for modelling of complex systems [52]. In proton therapy, the track of a single particle is simulated, rather than the whole beam of protons. Each event along the particle track is simulated based on the possible events and the relative possibilities. The statistical precision of the MC method is based on the number of primary particles in the simulation. Statistical uncertainty of MC simulations is given by $1/\sqrt{N}$, where N is the number of primary particles, and there are uncertainties related to the PDFs as well [53]. The calculation time increases as the accuracy increases, which is why treatment planning usually is performed with faster analytical calculation algorithms.

4.2 FLUKA

FLUKA is a code for simulation of particle transport and interaction [55-57]. It is a Monte Carlo code based on the programming language FORTRAN. A broad range of particles and energies can be simulated. It can be applied in several fields, including the field of medical physics. FLUKA simulations can be done in Flair, which is the belonging graphical user interface [58]. DICOM files can be imported into Flair and used as a basis for dose calculations.

4.3 Robust optimization

As mentioned in section 3.4, robust optimization was introduced to account for the shortcomings of the PTV in proton therapy. By including the range uncertainties of a proton beam in the treatment planning, the challenge of the PTV and margin concept

is handled. The geometrical uncertainties of proton therapy originate from motion, positioning and range uncertainties [13]. Robust optimization is introduced to increase the robustness of IMPT plans as well as to increase the sparing of OARs [59]. A way of performing robust optimization is shifting the dose distribution in three orthogonal directions and simultaneously apply the range uncertainty of e.g. ± 3 % [13]. This results in 12 scenarios, in addition to the original dose distribution. The optimization in proton therapy is based on minimizing a cost function $f(d)$, where d is the dose given by:

$$d_i = \sum_j D_{ij} x_j, \tag{14}$$

"where d_i is the dose in voxel i, x_j is the fluence of pencil beam j, and D_{ij} denotes the dose contribution of pencil beam j to voxel i." [[34], p. 92]. The geometric uncertainties are incorporated in D_{ij}, while x_j is without uncertainties. The two most common approaches to robust IMPT planning are the probabilistic approach and the worst-case approach. In the probabilistic approach the scenarios are weighted after the relative possibility of occurrence. The weighted sum of objective functions is minimized. The worst-case approach considers the "worst" scenario and aims to minimize the maximum objective function. The "worst" scenario is the dose distribution with voxels with maximum dose outside the target and the voxels with minimum dose inside the target [34].

5. Methods

The aim was to determine the potential to increase the biological dose to the BTV through biological optimization using proton therapy and simultaneously spare the OARs, as well as to explore the use of imaging to adapt target dose and to ensure tumor control while testing the optimization tool developed at the University of Bergen. To develop, validate and systematically investigate different optimization strategies, treatment optimization was first done on a simple water phantom. Subsequently, the most promising strategies were applied to a HNC patient cohort. The treatment plan of the water phantom was initially created in Eclipse Treatment Planning System (TPS) (Varian Medical Systems, Palo Alto, CA, USA) and further optimized in a FLUKA based optimization tool. The treatment plans of the HNC patient cohort were created in Eclipse TPS by Garrido-Hernandez et al. in a previous study and further optimized in this project [18].

5.1 FLUKA based optimization tool

The FLUKA based optimization tool is developed at the University of Bergen. Several features are included in the optimization tool, such as optimization of RBE-weighted dose, robust optimization and LET optimization. In this study, the tool was further developed to include ROWD optimization. The optimization tool offers 5 types of objectives that can be applied for structures in the treatment plan: Mean RBE-weighted dose or ROWD, maximum RBE-weighted dose or ROWD, minimum RBE-weighted dose or ROWD, maximum LET_d and minimum LET_d. The weight of each objective is defined by the user, as well as number of iterations, LET_d cut off value, α/β value and more. Robust optimization can be chosen for each objective, as well as calculation of ROWD. The optimization process is based on “worst-case” approach, as described in section 4.3. ROWD optimization was not an available feature of the optimization tool at the start of the project. As a result, ROWD was implemented in the optimization tool as a part of this thesis. The DAH model of OER as defined in equation (12) with the constants given in Table 1 was implemented in the code, together with a constant RBE of 1.1. The normoxic pO_2 was set to 160 mmHg, which is the standard normoxic pO_2

of *in vitro* studies. As a new argument was introduced to the optimization tool, the necessary code lines were modified to include the ROWD feature in various files. An aim of the implementation work was to ensure flexibility for the user. The user can choose any level of pO_2 up to 160 mmHg for the hypoxic structures. A structure is easily marked as hypoxic or normoxic. ROWD was also implemented in the scripts necessary for converting files from the optimization tool to DICOM files as well as files necessary for plotting DICOM files.

5.2 Treatment planning for the water phantom

The water phantom studied in this project is a cubical water phantom. A treatment plan was created for the water phantom in Eclipse TPS. Three structures were added to the water phantom, using the structure tools in Eclipse TPS, as shown in Figure 11. A CTV was added to the water phantom, a BTV was placed inside the CTV and an OAR was placed outside the CTV. The CTV structure is cropped such that the volume corresponding to the BTV is removed from the CTV volume. The cropped CTV is denoted zCTV. The IMPT plan consists of 3 fields, with degrees of 0°, 90° and 180°.

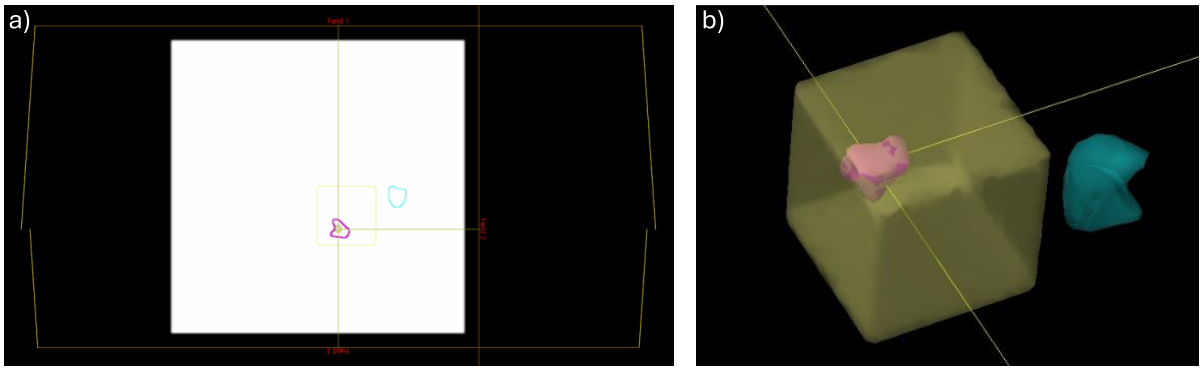

Figure 11: a) A cross section of the water phantom is shown in white together with the three incoming fields, b) A 3D illustration of the structures inside the water phantom. The zCTV is shown in yellow, the BTV is shown in pink and the OAR is shown in turquoise, while the yellow lines indicate incoming fields. The figures are from Eclipse TPS.

Prescribed dose for the zCTV is 2.0 Gy(RBE) and 2.2 Gy(RBE) for the BTV, while the maximum dose of the OAR is 0.50 Gy(RBE). The treatment plan was robust optimized in Eclipse. After exporting the treatment plan from Eclipse, the routine

described in section 5.3 was performed. The MC simulations of the water phantom in the optimization tool were done with 5000 primaries per pencil beam.

5.3 FLUKA-based dose calculation and optimization

The following method was used for both the water phantom treatment plan and the HNC patient plans.

After the treatment plan was exported from Eclipse, the FLUKA simulation environment was prepared. The DICOM files were sorted and the voxels outside the water phantom were set to vacuum. This was done to decrease the amount of unnecessary data for the simulation and reduce the calculation time. Regular optimization requires one voxel file, whereas robust optimization requires two additional voxel files to account for the range uncertainty of the proton beam. The voxel files were created in Flair by using files for calibration curves and material definition. The two additional voxel files were made with a calibration curve with ±3 % uncertainty. A calibration curve shows the relationship between CT Hounsfield units (HU) and electronic density. It is based on empirical data and is scanner dependent. Furthermore, the relevant regions of interest (ROI) were defined and chosen. The number of primary particles per pencil beam was initially set to 500 for the MC simulation of the water phantom, due to time efficiency in the initial testing. The number of primary particles per pencil beam was later increased to 5000, to ensure satisfactory statistics. MC simulations for both regular optimization and robust optimization was performed. Much of the initial testing was done with regular optimization. After achieving satisfying results with regular optimization, robust optimization was performed. This was done due to time efficiency, as the regular optimization runs faster than the robust optimization. The optimization process followed the MC simulations. The optimization objectives and corresponding weightings were modified between every optimization to successfully achieve the plan goals. Figure 12b) shows the setup of the objectives in the optimization tool belonging to an optimization of the water phantom. Furthermore, the optimization parameters were updated in a shell file, as shown in Figure 12a). The objectives and optimization

parameters varied between the different optimizations. Several files are generated in the optimization process, among them txt-files with dose and LET_d values for different volume percentages. The txt-files were used to plot DVH and LVH for the optimizations. Csv-files with metrics were also generated, and the median doses, median LET_d, near maximum doses ($D_{2\%}$) and near maximum LET_d ($LET_{d,2\%}$) were obtained from the metrics files. DICOM files of the optimizations were created and subsequently plotted.

```
PYTHON_SCRIPTS= #LOCATION OF PYTHON SCRIPTS
DICOM_LOCATION= #LOCATION OF DICOM FILES
LABEL= #LABEL OF OPTIMIZATION
python3 $PYTHON_SCRIPTS/python_optimizer.py \
-f scored_values.npz \
-l $LABEL \
-let_co 0.2 \
-its 100 \
-its_upd 3 \
-single \
-ro stochastic \
-ro_its 3 \
-para 3 \
-frac 20 \
-rowd 5.0 \
-dcm $DICOM_LOCATION

```

a)

	A	B	C	D	E	F
1	filenames:					
2	PTV_boost.dat	CTV_zBTV.dat	OAR.dat			
3	roi	p_d	weight	opt_type	robust	ROWD
4	0	2.2	50	1	0	0
5	1	2	1	1	1	0
6	2	0.5	1	2	0	0

b)

Figure 12: a) Shell file with optimization parameters of an optimization, b) “opt_params.csv” file, showing the optimization objectives of an optimization. See Appendix B for more details.

5.4 LET optimization of the water phantom

The optimization objectives were defined in a csv-file, as shown in Figure 12b). The LET_d cut off value was set to 0.2 Gy(RBE) per fraction for all optimizations in order to exclude LET_d contributions in regions of low dose. Many optimization strategies were tested, and the most promising ones are included in this thesis. Three different optimization strategies were compared, as specified in Table 2. The dose objectives were the same for all the different optimization strategies, only the LET_d objectives varied.

Table 2: Objectives of the optimization strategies.

Objectives	Optimization strategy		
	1	2	3
RBE-weighted dose boost to the BTV	X	X	X
Minimum LET_d of 5 keV/µm to the BTV		X	X
Maximum LET_d of 3 keV/µm to the OAR			X

To decide how the dose to the BTV should be defined, three methods were tested, as defined in Table 3. The goal was to achieve an equal dose to the BTV for all three optimization strategies. The different optimization strategies that were compared are defined in Table 2. All the objectives of method A, B and C have the same weight.

Table 3: Methods for defining dose to the BTV.

Method	Dose objective(s) to the BTV
A	Mean dose of 2.2 Gy(RBE)
B	Minimum dose of 2.2 Gy(RBE)
C	Minimum dose of 2.2 Gy(RBE) and maximum dose of 2.4 Gy(RBE)

After comparing the different methods, method A, using the objective of mean dose of 2.2 Gy(RBE) to the BTV was chosen for the rest of the simulations.

The optimization strategies were tested to investigate if it is possible to increase the LET_d to the BTV without affecting the OAR in a negative way when considering dose and LET_d. Various weighting alternatives for the objectives were tested, and the most promising were chosen. The weightings of the objectives are defined in Table 4. All three optimization strategies were robust optimized regarding the dose to the zCTV.

Table 4: Objectives and their weightings.

Objective	Weight
Mean dose of 2.2 Gy(RBE) to the BTV	50
Mean dose of 2.0 Gy(RBE) to the zCTV	1
Maximum dose of 0.50 Gy(RBE) to the OAR	1
Minimum LET_d of 5.0 to the BTV	50
Maximum LET_d of 3.0 to the OAR	1

5.5 ROWD optimization of water phantom

As previously mentioned, ROWD was implemented to account for the effect of tumor hypoxia with the optimization tool. Several optimization strategies and weightings of objectives were tested in order to achieve a homogeneous ROWD distribution to the relevant target volume. Two different strategies were compared to investigate the effect of hypoxia with the optimization tool. The first strategy assumes a hypoxic BTV and calculates the ROWD needed to account for the hypoxic effects (optimization A and B). The second strategy assumes a hypoxic BTV and gives a 10 % dose escalation to account for the hypoxic effects (optimization C). The pO_2 values of the BTVs of the first optimization strategy are 2.5 mmHg and 5.0 mmHg, while the second strategy use a pO_2 of 160 mmHg for the ROWD calculations, as the second strategy is based on dose escalation only and not ROWD optimization. The dose objectives are specified in Table 5 and in Table 6. All three optimizations were robustly optimized regarding the minimum dose to the zCTV.

Table 5: Objectives for optimization A and B.

Objective	Weight
Mean dose of 2.0 Gy(ROWD) to the BTV	50
Minimum dose of 1.95 Gy(ROWD) to the zCTV	1
Maximum dose of 2.05 Gy(ROWD) to the zCTV	1
Maximum dose of 0.50 Gy(ROWD) to the OAR	1

Table 6: Objectives for optimization C.

Objective	Weight
Mean dose of 2.2 Gy(ROWD) to the BTV	50
Minimum dose of 1.95 Gy(ROWD) to the zCTV	1
Maximum dose of 2.05 Gy(ROWD) to the zCTV	1
Maximum dose of 0.50 Gy(ROWD) to the OAR	1

5.6 ROWD optimization of HNC patient plans

The HNC patient cohort studied in this thesis is a part of the EMINENCE study (NCT04612075). The study is approved by the Regional Committee for Medical Research Ethics in Central Norway (approval number: 2019/64744). All patients have locally advanced squamous cell carcinoma. The patient cohort were treated with volumetric modulated arc therapy (VMAT) with photons. The prescribed dose to the PTV and CTV of high risk was 68 Gy, delivered in 34 fractions over 6 weeks. PTVs and CTVs of intermediate and lower risk were prescribed a lower dose. The target volumes were delineated based on CT images. The BTV structures were delineated based on comparison of baseline and interim PET images by using the semiautomatic just-enough-interaction method by Garrido-Hernandez et al. in a previous study [18, 60]. The interim MRI/PET images were taken 13 – 15 days after the start of the treatment. The radiotracer ^{18}F-FDG was used in the PET scan and the imaging was performed in treatment position. IMPT plans for the HNC patient cohort were created

in Eclipse. The positions were head-first supine, with 10 cm distance in air between the snout and the skin of the patient. The original prescribed doses from the VMAT treatment plans were used as objectives for the new IMPT plans, and a constant RBE of 1.1 was used. The treatment plans had three and five fields for unilateral and bilateral CTVs, respectively. Range shifters were used in the treatment plans. Furthermore, the treatment plans were MC simulated with FLUKA, using $5 \cdot 10^7$ primary particles per field, as described in section 5.3.

The work performed in the former paragraph was done in earlier studies [18]. The following paragraph describes the work done in this project. 5 patient plans are studied in this thesis. All treatment plans were optimized with the optimization tool. As for the ROWD optimization of the water phantom, two optimization strategies were compared for each patient. The first strategy assumes a hypoxic BTV and calculates the ROWD needed to account for the hypoxic effects. The second strategy assumes a hypoxic BTV and gives a 10 % dose escalation to account for the hypoxic effects. The pO_2 values of the BTVs of the first optimization strategy are 2.5 mmHg and 5.0 mmHg, while the second strategy use a pO_2 of 160 mmHg for the ROWD calculations. The ROWD optimization and dose escalation is performed with DPBC. The prescribed dose of the BTVs with pO_2 of 2.5 mmHg and 5.0 mmHg is 68 Gy(ROWD), while the prescribed dose of the dose escalated BTVs is 74.8 Gy(ROWD). The prescribed dose of the CTVs is 68 Gy(ROWD). The HNC patient plans were normalized to 68 Gy(RBE) for a belonging PTV. The dose constraints of the OARs are adopted from the treatment plans of the earlier studies, which are based on the Danish Head and Neck Cancer (DAHANCA) 2020 guidelines [61]. The dose constraints of the pharynx mucosa are based on [62]. 22 fractions were optimized with ROWD optimization and dose escalation to the hypoxic and dose escalated BTVs, respectively. The number of iterations was set to 100 and the α/β value was set to 3.76 Gy for all optimizations. Several optimization strategies were investigated to achieve a homogeneous ROWD in the relevant target volumes. The results were considered as satisfying when the median dose of the BTVs was within prescribed dose ± 0.50 Gy(ROWD). After achieving satisfying results, the optimized treatment plans of the 22 fractions were converted to

DICOM. Subsequently, the DICOM files of the 22 fractions were combined with the DICOM files of the first 12 fractions, which do not include ROWD optimization or dose escalation. Txt-files with dose and LET_d data were created from the DICOM files and later plotted as color washes, DVH, LVH and box plots. The CTV structures that have a BTV on the inside are cropped such that the volume corresponding to the BTV is removed from the CTV volume. The CTVs of the patient plans are denoted zCTV.

6. Results

6.1 LET optimization of the water phantom

The DVH, LVH and color wash plots of the water phantoms comparing the optimization strategies as defined in Table 4 are shown in Figure 13-15. The first optimization strategy includes dose escalation to the BTV (DE), the second optimization strategy includes dose and LET_d escalation to the BTV (DE-LET_{BTV}), and the third optimization strategy includes dose and LET_d escalation to the BTV as well as LET_d restriction to the OAR (DE-$LET_{BTV, OAR}$).

The DVH in Figure 13a) shows that the doses are relatively similar for all three optimization strategies, although the graphs for the BTV of the DE-LET_{BTV} and DE-$LET_{BTV, OAR}$ strategies are less steep than for the DE strategy. As the slope indicates the homogeneity of the dose distribution of a structure, this indicates that the DE strategy results in a more homogeneous dose distribution of the BTV. This is confirmed when looking at the color wash plots of RBE-weighted dose in Figure 14. Still, the median doses of the BTVs of the different optimization strategies are relatively similar, as seen in Table 7. The median doses of the BTVs do however not reach the goal of 2.2 Gy(RBE), all the values are slightly below the goal. This might be due to the prescribed dose of 2.0 Gy(RBE) to the zCTVs. There is a physical limitation of how steep the dose gradient can be. The median doses of the zCTVs are identical and all reach the goal of 2.0 Gy(RBE), and there is no significant difference in the $D_{2\%}$ values (Table 7). As seen in the color wash plots of the RBE-weighted dose in Figure 14, the dose of the zCTV of the DE strategy appears to be more homogeneous compared to the zCTVs of the DE-LET_{BTV} and DE-$LET_{BTV, OAR}$ strategies. All three optimization strategies have a similar tail of the zCTV dose (Figure 13a), which may originate from the small rim of elevated dose observed around the BTVs (Figure 14). The $D_{2\%}$ of the BTVs and OARs increase slightly when including LET_d objectives (Table 7), and is slightly above the maximum dose objective of the OAR for all three optimization strategies. However, the OAR doses are below the maximum objective of 0.50 Gy(RBE) for most of the OAR volumes (Figure 13a). The OAR dose of the DE strategy is generally lower than

the DE-LET$_{BTV}$ and DE-LET$_{BTV,\ OAR}$ strategies, although the difference is not large. The similarity between the OAR doses of the three optimization strategies is also seen in the color wash plots of the RBE-weighted dose in Figure 14. As the cut off value of the RBE-weighted dose in the color wash plots are at 0.2 Gy(RBE), one can observe how large parts of the OARs do not receive dose above this value.

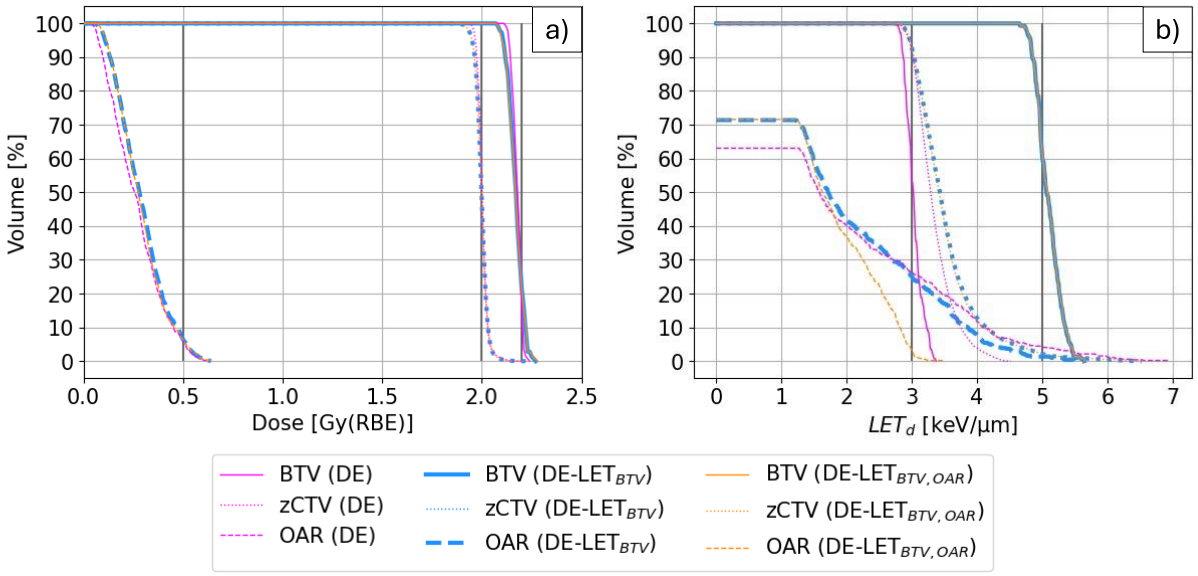

Figure 13: a) DVH comparing the different optimization strategies, b) LVH comparing the different optimization strategies. The graphs of the DE-LET $_{BTV,\ OAR}$ strategy is on top of the graphs of the DE-LET $_{BTV}$ strategy in some parts of the plots. The vertical grey lines in the DVH and LVH indicate the dose and LET$_d$ goals.

While the doses of the BTVs are similar, there is a significant difference in the LET$_d$ of the BTVs between the different strategies. The LET$_d$ of the BTVs corresponding to the DE-LET$_{BTV}$ and DE-LET$_{BTV,\ OAR}$ strategies appear nearly identical and are significantly higher compared to the DE strategy (Figure 13b). The median LET$_d$ of the BTVs of the DE-LET$_{BTV}$ and DE-LET$_{BTV,\ OAR}$ strategies are increased by approximately 2.0 keV/µm, compared to the DE strategy, and thus achieving the goal of median 5.0 keV/µm to the BTV (Table 8).

The difference in LET$_d$ can also be seen in the color wash plots of the LET$_d$ distribution in Figure 15, which clearly show how the LET$_d$ is increased in the BTV and in the area around it for the DE-LET$_{BTV}$ and DE-LET$_{BTV,\ OAR}$ strategies. Their LET$_d$ distributions do however not appear very homogeneous. This is confirmed by looking at the LET$_d$

of the BTVs corresponding to the DE-LET_{BTV} and DE-$LET_{BTV, OAR}$ strategies in the LVH in Figure 13b). Comparing the near maximum LET_d ($LET_{d,2\%}$) to the median LET_d of the BTVs also supports the observation of inhomogeneity. The $LET_{d,2\%}$ of the BTV is increased by approximately 2.2 keV/µm for the DE-LET_{BTV} and DE-$LET_{BTV, OAR}$ strategies, compared to the DE strategy.

Table 7: Median doses and $D_{2\%}$ of the structure in the water phantom for the different optimization strategies.

Structure	Optimization strategy	Median dose (Gy(RBE))	$D_{2\%}$ (Gy(RBE))
BTV	DE	2.18	2.22
	DE-LET_{BTV}	2.17	2.24
	DE-$LET_{BTV, OAR}$	2.17	2.24
zCTV	DE	2.00	2.07
	DE-LET_{BTV}	2.00	2.06
	DE-$LET_{BTV, OAR}$	2.00	2.06
OAR	DE	0.26	0.54
	DE-LET_{BTV}	0.28	0.56
	DE-$LET_{BTV, OAR}$	0.28	0.57

Table 8: Median LET_d and $LET_{d,2\%}$ of the structures in the water phantom for the different optimization strategies.

Structure	Optimization strategy	Median LET_d (keV/µm)	$LET_{d2\%}$ (keV/µm)
BTV	DE	3.02	3.32
	DE-LET_{BTV}	5.06	5.47
	DE-$LET_{BTV, OAR}$	5.08	5.48
zCTV	DE	3.29	4.17
	DE-LET_{BTV}	3.43	5.04
	DE-$LET_{BTV, OAR}$	3.42	5.04
OAR	DE	1.59	5.73
	DE-LET_{BTV}	1.71	4.72
	DE-$LET_{BTV, OAR}$	1.63	3.03

As seen in the LVH in Figure 13b), the LET_d of the zCTVs is generally higher for the optimization strategies which include LET_d objectives, namely the DE-LET_{BTV} and DE-$LET_{BTV, OAR}$ strategies. This is also seen in the values of median LET_d and $LET_{d,2\%}$ in Table 8. The $LET_{d,2\%}$ of the zCTV is increased by approximately 0.87 keV/µm for the DE-LET_{BTV} and DE-$LET_{BTV, OAR}$ strategies, compared to the DE strategy. The color wash plots of LET_d in Figure 15 show an area of increased LET_d around the BTV for the DE-$LET_{BTV,}$ and DE-$LET_{BTV, OAR}$ strategies.

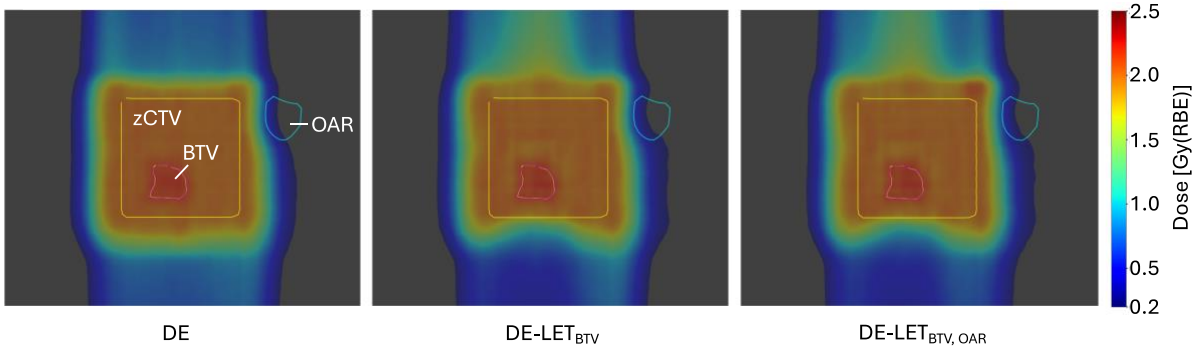

Figure 14: RBE-weighted dose distributions of the water phantom for the three optimization strategies. The BTV is shown in pink, the zCTV is shown in yellow and the OAR is shown in turquoise.

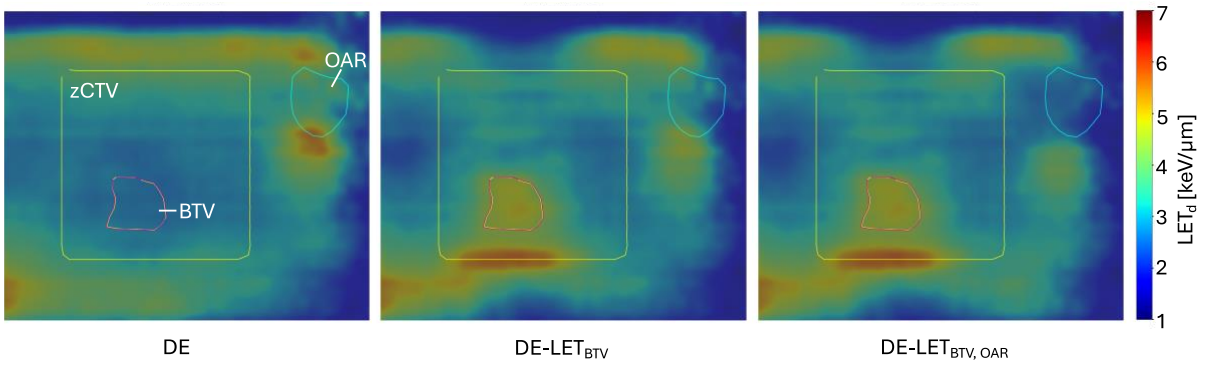

Figure 15: LET_d distribution of the water phantom for the different optimization strategies. The BTV is shown in pink, the zCTV is shown in yellow and the OAR is shown in turquoise.

While the doses of the OARs are similar, the values of the LET_d vary. The LVH in Figure 13b) shows how the DE-$LET_{BTV, OAR}$ strategy results in a significantly lower LET_d of the OAR compared to the DE and DE-LET_{BTV} strategies. Only a small percentage of the OAR volume receives LET_d above the maximum constraint of 3.0 keV/µm to the OAR for the DE-$LET_{BTV, OAR}$ strategy. Considering the LVH in Figure 13b), the LET_d distribution of the OARs appear to be more inhomogeneous for the DE and DE-LET_{BTV} strategies, compared to the DE-$LET_{BTV, OAR}$ strategy. The difference between the values of median LET_d and $LET_{d,2\%}$ of the OARs are greater for the DE and DE-LET_{BTV} strategies than for the DE-$LET_{BTV, OAR}$ strategy. This is in accordance with the inhomogeneity that was observed in the LVH. The color wash plots of the LET_d in Figure 15 shows a clear difference between the OARs of the different optimization strategies. The OAR of the DE strategy appears to have higher values of LET_d in the majority of the volume, compared to the two other optimization strategies. The OAR of the DE-$LET_{BTV, OAR}$ strategy has significantly lower LET_d in the whole volume.

Dose escalation of the BTV was successful for all three optimization strategies, although the goal of mean dose was not achieved completely. This might be due to a conflicting objective of mean dose to the zCTV. The LET_d was successfully escalated in the BTV for both the DE-LET_{BTV} and DE-$LET_{BTV, OAR}$ strategies, and the LET_d of the OAR was significantly lower for the DE-$LET_{BTV, OAR}$ strategy. The LET_d escalation in the BTV and LET_d restriction of the OAR did not have a noteworthy effect on the

dose delivery. The results indicate that the optimization tool has the potential for both dose escalation and LET_d optimization in a smaller volume.

6.2 ROWD optimization of water phantom

The DVH, LVH and color wash plots of the water phantom comparing the cases with various pO_2 of the BTV as defined in Table 5 and Table 6 are shown in Figure 16-19. As defined in section 5.5, two strategies are compared. The first strategy assumes a hypoxic BTV and calculates the ROWD needed to account for the hypoxic effects. The second strategy assumes a hypoxic BTV and gives a 10 % dose escalation to account for the hypoxic effects. The pO_2 values of the BTVs of the first optimization strategy are 2.5 mmHg and 5.0 mmHg, while the second strategy uses a pO_2 of 160 mmHg for the ROWD calculations. The prescribed dose of the BTVs with pO_2 of 2.5 mmHg and 5.0 mmHg is 2.0 Gy(ROWD), while the prescribed dose of the dose escalated (DE) BTV is 2.2 Gy(ROWD).

The DVH in Figure 16a) shows how the DE BTV receives a homogeneous ROWD of 2.2 Gy(ROWD). The ROWD of the BTVs with pO_2 of 2.5 mmHg and 5.0 mmHg are relatively similar, but slightly less homogeneous than the DE BTV. However, the homogeneity does not appear to differ significantly when considering the color wash plots of the ROWD distribution in Figure 18. All three BTVs achieve the goals of their objectives, and the median ROWDs of the BTVs with pO_2 of 2.5 mmHg and 5.0 mmHg are identical (Table 9).

In the DVH in Figure 16a) one can observe how the RBE-weighted dose of the BTVs with pO_2 of 2.5 mmHg and 5.0 mmHg are significantly higher than the corresponding ROWD with a median RBE-weighted dose of 2.98 Gy(RBE) and 2.56 Gy(RBE) for the BTVs with pO_2 of 2.5 mmHg and 5.0 mmHg, respectively. Similarly, the $D_{2\%}$ of the BTVs with pO_2 of 2.5 mmHg and 5.0 mmHg are 3.14 Gy(RBE) and 2.68 Gy(RBE), respectively. The same increase in RBE-weighted dose is seen in the color wash plots of RBE-weighted dose distribution in Figure 17. The median OER of the BTVs with pO_2 of 2.5 mmHg and 5.0 mmHg are 1.49 and 1.28 corresponding to 2.5 mmHg and

5.0 mmHg, respectively, when calculated for the median RBE-weighted doses and ROWD. As the OER of normoxic tissue is 1, ROWD equals RBE-weighted dose for the DE BTV. Hence, the color wash plots of the RBE-weighted dose and ROWD in Figure 17 and Figure 18, respectively, are equal for the DE case.

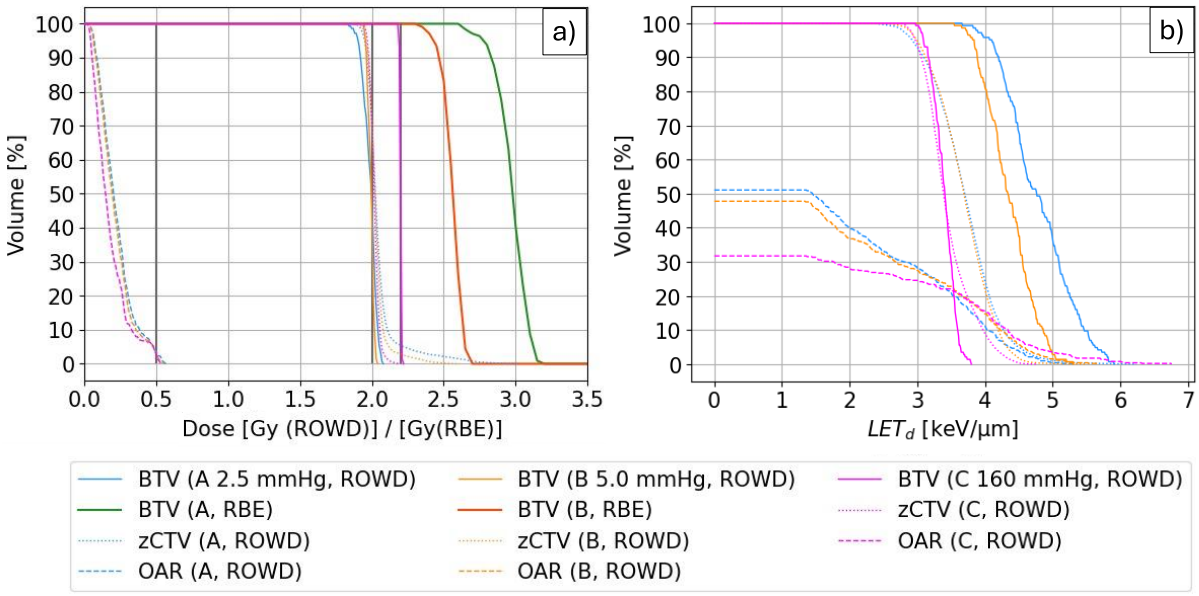

Figure 16: a) DVH for the water phantom with various pO_2 values of the BTVs, b) LVH for the water phantom with various pO_2 values of the BTVs. The grey vertical lines indicate dose goals.

The doses of the zCTVs are relatively similar, as shown in the DVH in Figure 16a). The maximum doses of the zCTVs increase with decreasing pO_2 of the corresponding BTV. The $D_{2\%}$ is increased by 0.43 Gy(ROWD) and 0.17 Gy(ROWD) of the zCTVs corresponding to the BTVs of 2.5 mmHg and 5.0 mmHg, respectively, compared to the $D_{2\%}$ of the zCTV corresponding to the DE BTV (Table 9). There is a rim of elevated dose around the BTVs with pO_2 of 2.5 mmHg and 5.0 mmHg inside the zCTVs, as seen in the color wash plots of the ROWD distribution in Figure 18. The dose of the rim is highest for the zCTV corresponding to the most hypoxic BTV. The rims may cause the increase in maximum dose of the zCTVs with decreasing pO_2 of the BTV.

The OAR doses are mostly below the maximum constraint of 0.50 Gy(ROWD) for all three cases (Figure 16a). The doses of the OARs corresponding to the BTVs with pO_2 of 2.5 mmHg and 5.0 mmHg are nearly identical and are slightly higher than the dose of the OAR corresponding to the DE BTV (Table 9). The color wash plots of RBE-

weighted dose and ROWD in Figure 17 and Figure 18, respectively, show similar doses to the different OARs.

Table 9: Median dose and $D_{2\%}$ of the BTV, zCTV and the OAR for the different cases.

Structure	pO_2 of BTV (mmHg)	Median dose (Gy(ROWD))	$D_{2\%}$ (Gy(ROWD))
BTV	2.5	2.00	2.06
	5.0	2.00	2.03
	160	2.20	2.21
zCTV	2.5	2.02	2.52
	5.0	2.02	2.26
	160	2.02	2.09
OAR	2.5	0.20	0.53
	5.0	0.19	0.51
	160	0.15	0.50

Table 10: Median LET_d and $LET_{d,2\%}$ of the BTV, zCTV and the OAR for the different cases.

Structure	pO_2 of BTV (mmHg)	Median LET_d (keV/µm)	$LET_{d2\%}$ (keV/µm)
BTV	2.5	4.76	5.81
	5.0	4.34	5.04
	160	3.41	3.71
zCTV	2.5	3.70	4.79
	5.0	3.69	4.48
	160	3.39	4.31
OAR	2.5	1.45	4.71
	5.0	0.00	4.91
	160	0.00	5.31

There are large differences in LET_d of the BTVs with different pO_2. The general trend, as seen in the LVH in Figure 16b), is increasing LET_d with decreasing pO_2. The DE BTV has a median LET_d of 3.41 keV/µm, and it was increased by 1.35 keV/µm and 0.93 keV/µm for the BTVs with pO_2 of 2.5 mmHg and 5.0 mmHg, respectively (Table 10). The same trend of increasing LET_d with decreasing pO_2 can be observed in the color wash plots of the LET_d distribution, as shown in Figure 19. The zCTVs corresponding to the BTVs with pO_2 of 2.5 mmHg and 5.0 mmHg have large areas of elevated LET_d around the BTVs, compared to the zCTV corresponding to the DE BTV. None of the zCTVs appear homogeneous when considering the color washes of the LET_d distribution. The median LET_d of the zCTVs corresponding to the BTVs with pO_2 of 2.5 mmHg and 5.0 mmHg are nearly identical and are approximately 0.30 keV/µm higher than the median LET_d of the zCTV corresponding to the DE BTV (Table 10).

While the doses of the OARs are similar, the LET_d of the OARs shows more variation. The LVH in Figure 16b) indicates an inhomogeneous LET_d distribution of the OARs. This is confirmed by considering the color wash plots of the LET_d distributions in Figure 19. The LET_d distribution of the OAR corresponding to the DE BTV appears to be more inhomogeneous and has a higher level of maximum LET_d compared to the OARs corresponding to the BTVs with pO_2 of 2.5 mmHg and 5.0 mmHg (Figure 19). The trend can also be observed by looking at the values of $LET_{d,2\%}$ of the OARs in Table 8.

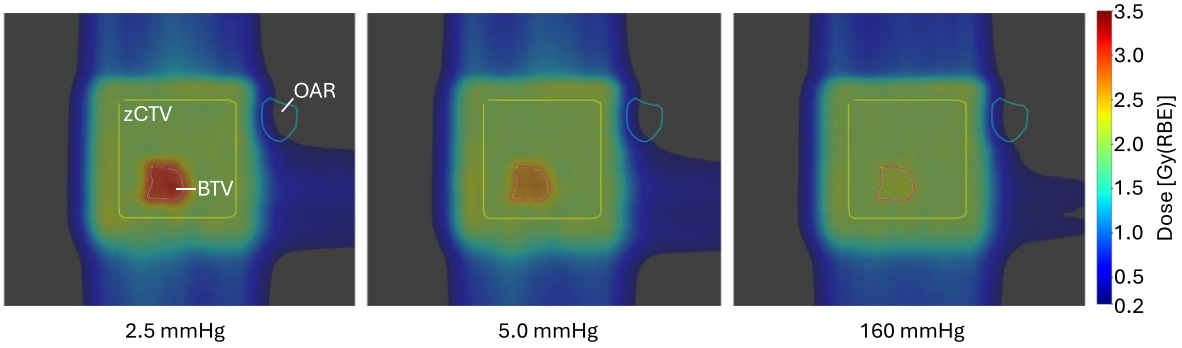

Figure 17: RBE-weighted dose distributions of the water phantoms with various pO_2 values of the BTVs. The BTV is shown in pink, the zCTV is shown in yellow and the OAR is shown in turquoise.

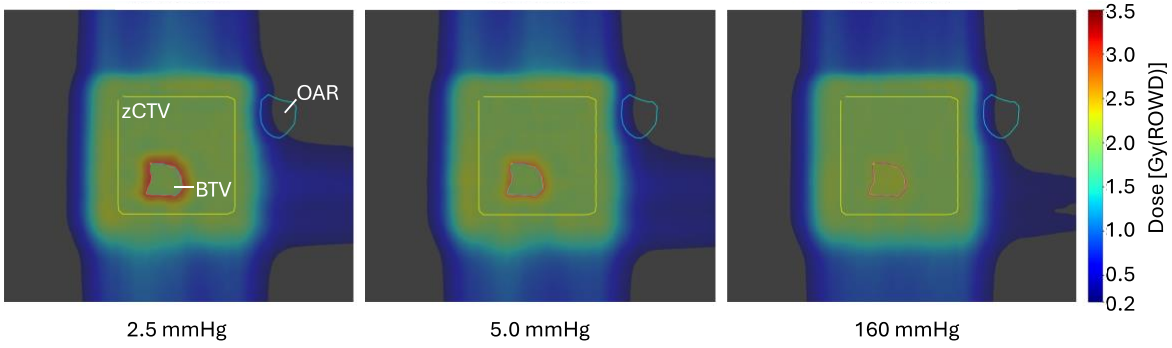

Figure 18: RBE and OER weighted dose distributions of the water phantoms with various pO_2 values of the BTVs. The BTV is shown in pink, the zCTV is shown in yellow and the OAR is shown in turquoise.

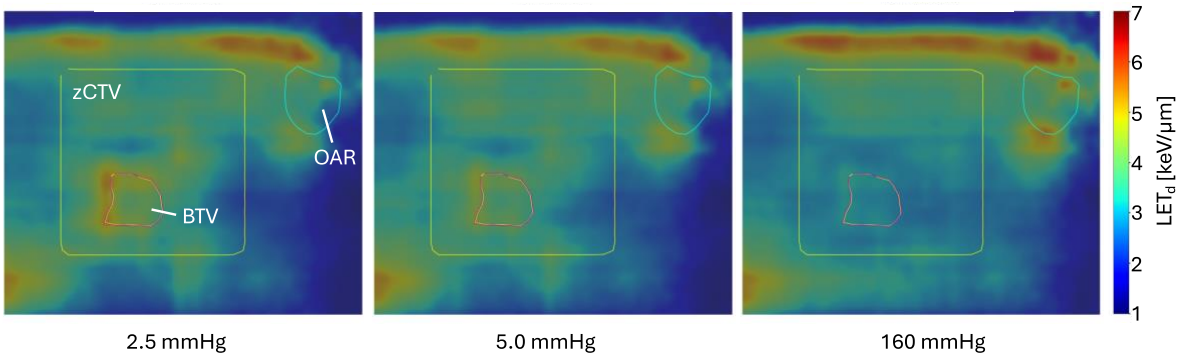

Figure 19: LET_d distributions of the water phantoms with various pO_2 values of the BTVs. The BTV is shown in pink, the zCTV is shown in yellow and the OAR is shown in turquoise. There is no LET_d cut-off value, as opposed to the LVH in Figure 13b).

6.3 ROWD optimization of HNC patient plans

As defined in section 5.6, two strategies are compared. The first strategy assumes a hypoxic BTV and calculates the ROWD needed to account for the hypoxic effects. The second strategy assumes a hypoxic BTV and gives a 10 % dose escalation to account for the hypoxic effects. The pO_2 values of the BTVs of the first optimization strategy are 2.5 mmHg and 5.0 mmHg, while the second strategy uses a pO_2 of 160 mmHg for the ROWD calculations. The prescribed dose of the BTVs with pO_2 of 2.5 mmHg and 5.0 mmHg is 68 Gy(ROWD), while the prescribed dose of the DE BTV is 74.8 Gy(ROWD).

The ROWD optimization resulted in similar ROWD and relatively homogeneous ROWD to the BTVs both for 2.5 mmHg and 5.0 mmHg (Figure 20). This indicates successful ROWD optimization. As seen in the DVH in Figure 20, the ROWD (solid lines) of the BTVs of pO_2 2.5 mmHg and 5.0 mmHg were achieved by increasing the RBE-weighted dose (dashed lines) significantly. The mean median RBE-weighted dose of the DE BTVs is 74.10 Gy(RBE), which is slightly below the prescribed dose. The mean median RBE-weighted doses are increased by 17.58 Gy(RBE) and 7.08 Gy(RBE) for the BTVs with pO_2 of 2.5 mmHg and 5.0 mmHg, respectively, compared to the DE BTV. The increase in RBE-weighted dose with decreasing pO_2 can also be seen in the color wash plots of RBE-weighted dose in Figure 26. The increase in RBE-weighted dose is as expected, due to hypoxia. The median OER is 1.34 and 1.20 of the BTVs with pO_2 of 2.5 mmHg and 5.0 mmHg, respectively, calculated from the mean median RBE-weighted dose and ROWD. These values correspond well with the relative increase in RBE-weighted dose observed from the ROWD optimization.

There is some variation between the ROWD of the BTVs of the same level of pO_2, which can be observed in both the box plot of median ROWD in Figure 22 and in the DVH in Figure 20. However, the differences are not large and the ROWD of the BTVs with pO_2 of 2.5 mmHg and 5.0 mmHg are relatively similar. The DE BTVs showed the most variation between the BTV doses, as seen in the DVH, which is confirmed when looking at the box plot of median ROWD. All the DE BTVs appear relatively

homogeneous when considering the DVH and the color wash plots of ROWD distribution in Figure 27. The HNC patient plans are normalized to 68 Gy(RBE) of a normoxic PTV structure, which is not included in the plots.

While the RBE-weighted dose differs between the BTVs of different pO_2, the LVH in Figure 21 shows that the LET_d of the BTVs are somewhat similar for most patients. The box plot of median LET_d in Figure 24 shows that the variation is relatively small, and the mean median LET_d is around 2.55 keV/µm for BTVs of all pO_2. The color wash plots of LET_d distribution in Figure 28 show no significant differences between the BTVs of different pO_2.

In the box plot of $D_{2\%}$ in Figure 23 one can see how the $D_{2\%}$(ROWD) of the BTVs with pO_2 of 2.5 mmHg is higher than the $D_{2\%}$(ROWD) of the BTVs with pO_2 of 5.0 mmHg. The $D_{2\%}$(ROWD) is highest for the DE BTVs, which is logical as the DE BTVs have a higher prescribed ROWD. The $D_{2\%}$(ROWD) varied most for the DE BTVs. The $D_{2\%}$(RBE) of the BTVs is increasing significantly with decreasing pO_2, as expected.

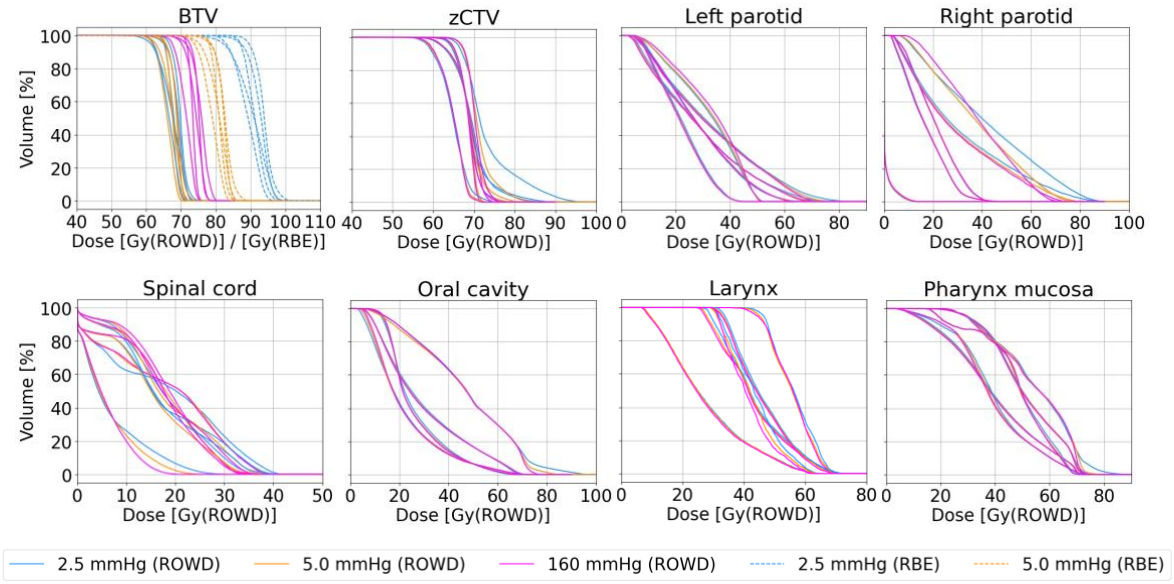

Figure 20: DVH of the BTV, zCTV and relevant OARs of the patient plans. Both ROWD and RBE-weighted dose are shown along the x-axis in the DVH of the BTV. The solid lines indicate ROWD and the dashed lines indicate RBE-weighted while the different colors of the graphs correspond to different values of pO_2 of the corresponding BTV.

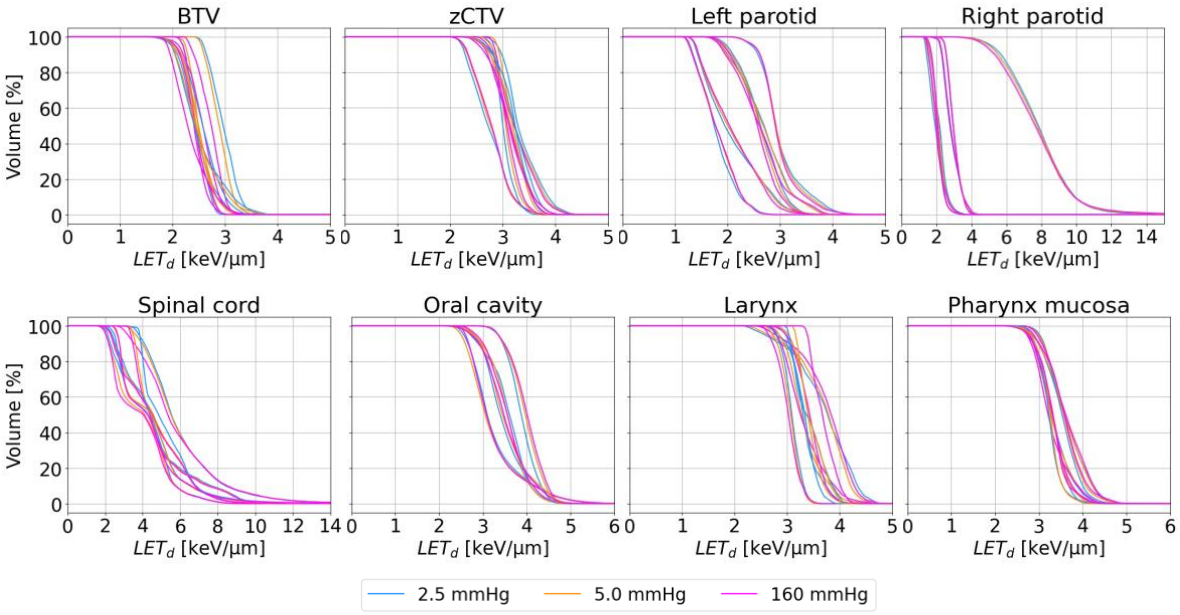

Figure 21: LVH of the BTV, zCTV and relevant OARs of the patient plans. The different colors of the graphs correspond to different values of pO_2 of the corresponding BTV.

The DVH in Figure 20 shows that the doses of the zCTVs are relatively similar, while some zCTVs receive less dose than prescribed and some zCTVs receive higher levels of maximum dose. The zCTVs appear relatively homogeneous when considering the DVH, but one zCTV corresponding to a BTV with pO_2 of 2.5 mmHg receives high values of dose in larger parts of the volume compared to the rest of the zCTVs. The color wash plots of ROWD distribution in Figure 27 show a rim of higher dose around the hypoxic BTVs, which explains the elevated dose in certain parts of the volume as seen in the DVH. As seen in the color wash plots of ROWD distribution, the dose is highest around the most hypoxic BTV. The median dose of the zCTVs appear relatively similar, as seen in the box plot in Figure 22, with a small increase of median dose with decreasing pO_2 of the corresponding BTVs. The mean median dose does however not differ significantly between the zCTVs with different pO_2 of the corresponding BTVs and is approximately 68.5 – 68.8 Gy(ROWD). Some patients had several zCTVs, and not all of them had a BTV inside. Hence, not all zCTVs receive a high dose contribution from the BTV. This may explain the difference in homogeneity as seen in the DVH in Figure 20. The box plot of $D_{2\%}$ in Figure 23 shows that the $D_{2\%}$ of the zCTVs varies more with decreasing pO_2 of the corresponding BTV. The median $D_{2\%}$ increase with

decreasing pO_2. This is in accordance with the rim of high dose observed in the color wash plots of ROWD distribution.

The LVH in Figure 21 shows that the homogeneity of the LET_d of the zCTVs differ, while the median LET_d is relatively similar. The box plot of median LET_d shows a small increase of median LET_d of the zCTVs with decreasing pO_2 of the corresponding BTV, and the variation is increasing with decreasing pO_2 of the BTV. The mean median LET_d of the zCTVs is around 3.1 keV/µm. The color wash plots of LET_d distribution in Figure 28 do not show any significant difference between the zCTVs. The zCTVs corresponding to the BTVs with pO_2 of 2.5 mmHg have more variation in the values of median LET_d. The $LET_{d,2\%}$ of the zCTVs are relatively similar, as seen in the box plot in Figure 25.

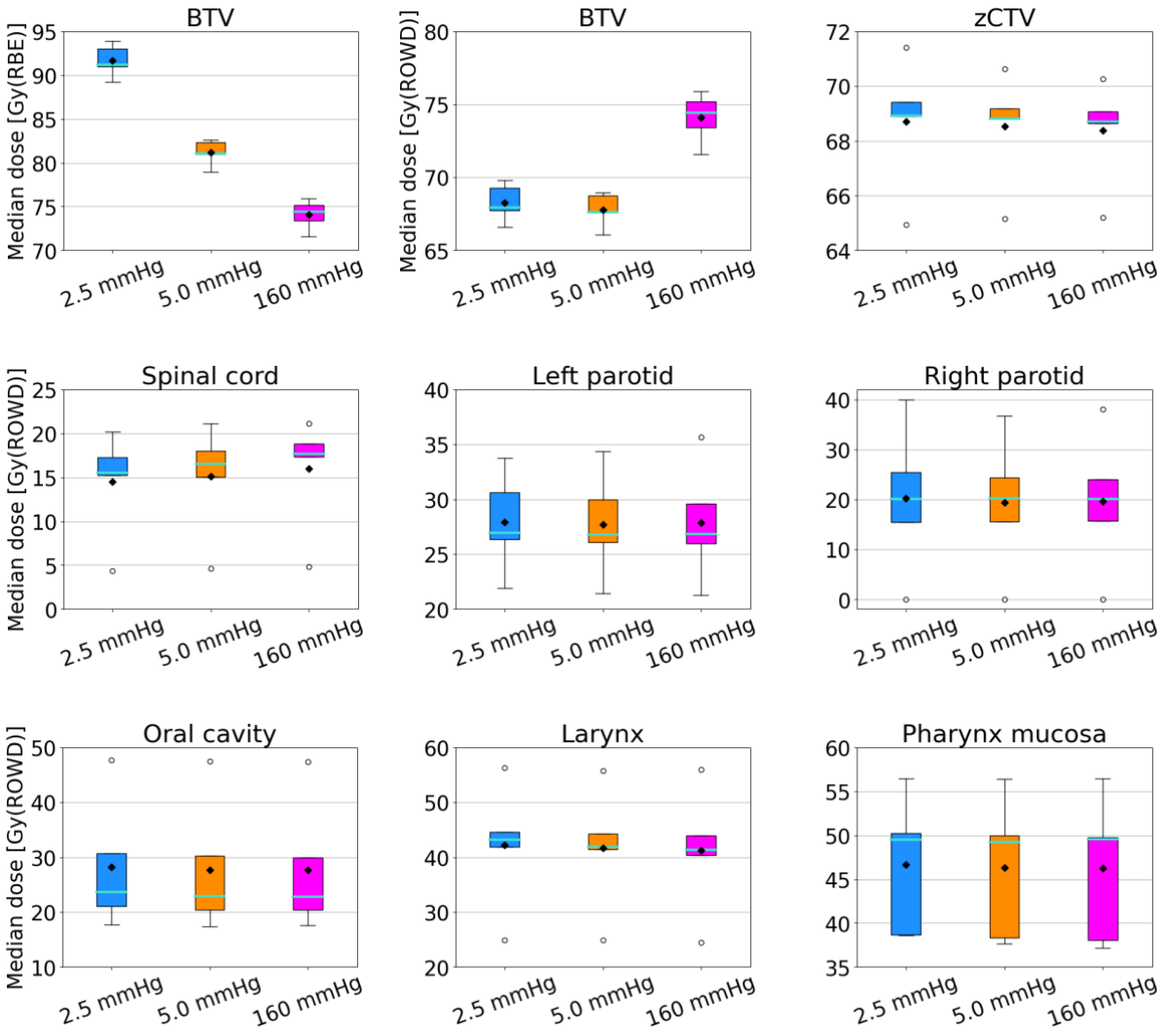

Figure 22: Box plots of the median dose of different structures of the patient plans. The turquoise lines indicate the median value, the black diamond shapes indicate the mean value and the black circles indicate outliers.

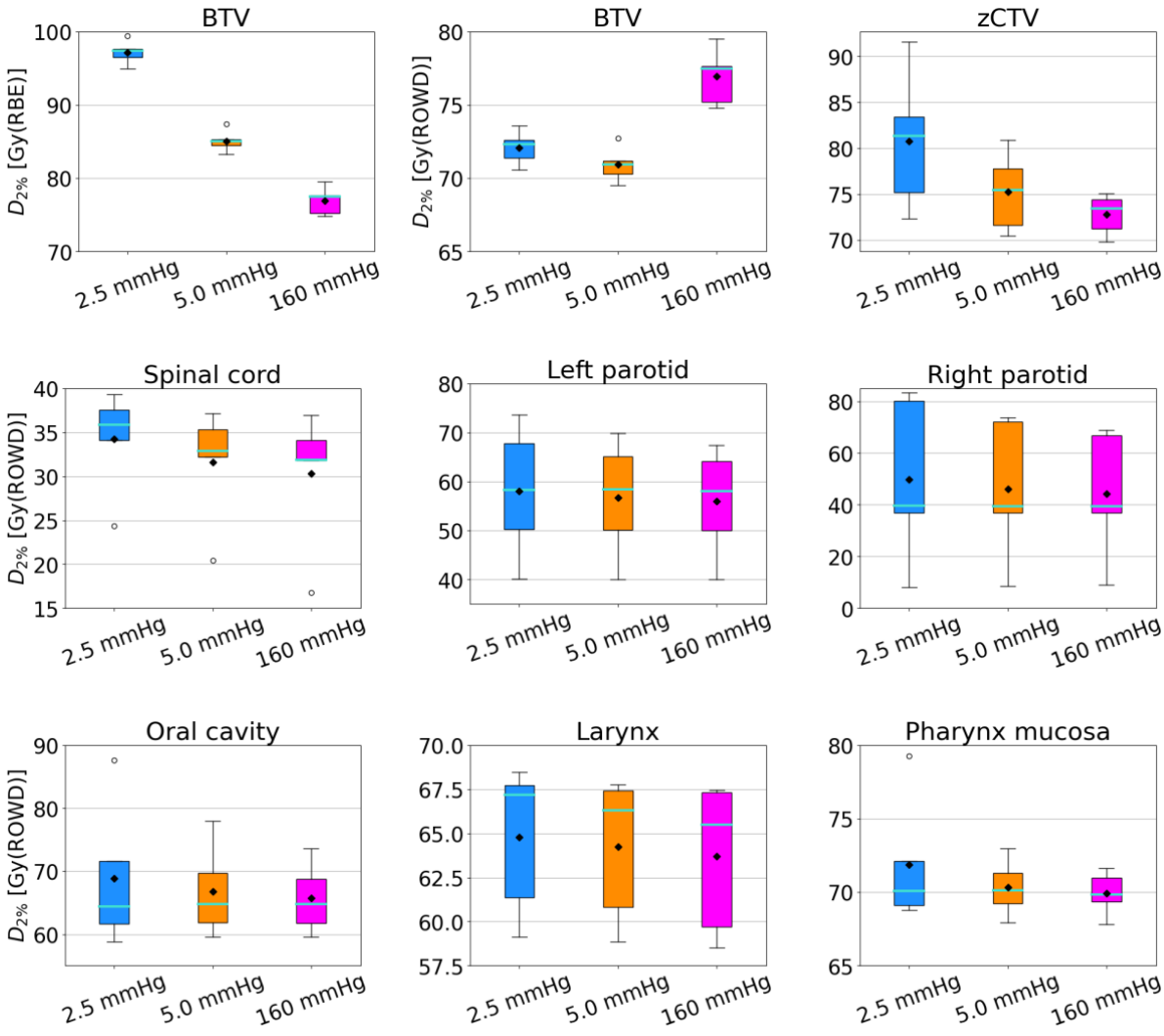

Figure 23: Box plots of the $D_{2\%}$ of different structures of the patient plans. The turquoise lines indicate the median value, the black diamond shapes indicate the mean value and the black circles indicate outliers.

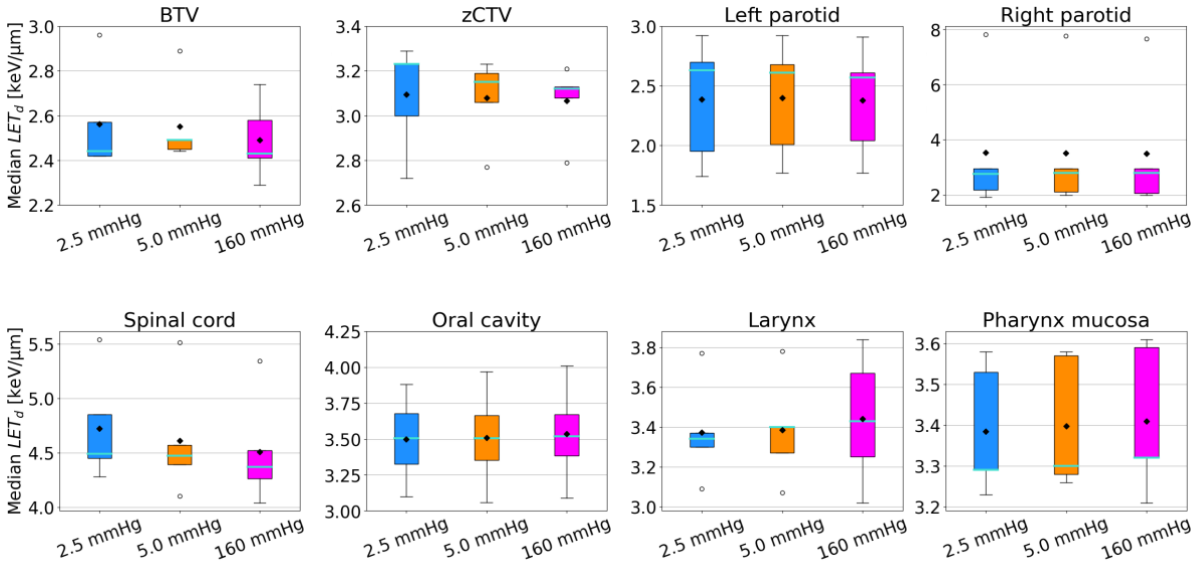

Figure 24: Box plot of the median LETd of different structures of the patient plans. The turquoise lines indicate the median value, the black diamond shapes indicate the mean value and the black circles indicate outliers.

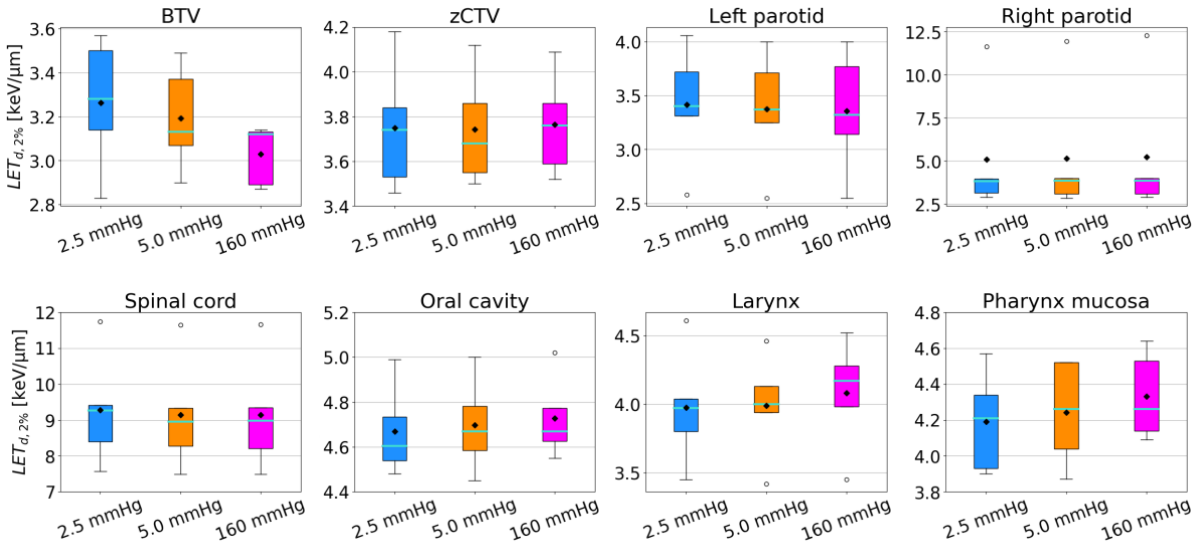

Figure 25: Box plot of the $LET_{d2\%}$ of different structures of the patient plans. The turquoise lines indicate the median value, the black diamond shapes indicate the mean value and the black circles indicate outliers.

The pO_2 of the corresponding BTV does not appear to have a noteworthy effect on dose of the OARs, when considering the DVH (Figure 20). This is confirmed when looking at the box plots of median ROWD and $D_{2\%}$ of the OARs in Figure 22 and Figure 23, respectively. As seen in the color wash plots of ROWD distribution in Figure 26, one can observe that parts of the left parotid, pharynx mucosa and oral cavity receive high dose due to the rim of high dose around the BTV with pO_2 of 2.5 mmHg. The rim of

elevated dose around the hypoxic BTVs are a reason for differences in dose of the OARs. Figure 21 shows the LVH of the OARs. As for the dose, the level of pO_2 of the corresponding BTVs do not appear to have a noteworthy effect on the LET_d of the OARs. This is also seen in the box plots of median LET_d and $LET_{d2\%}$ in Figure 24 and Figure 25, respectively. There is no general trend of increase or decrease of neither dose nor LET_d of the OARs depending on the pO_2 of the BTV.

Table 11: Colors of the structures in the color wash plots in Figure 26, Figure 27 and Figure 28.

Structure	BTV	zCTV	Parotids	Oral cavity	Pharynx mucosa	Spinal cord
Color	Light beige	Pink	Light green	Yellow	Dark green	Blue

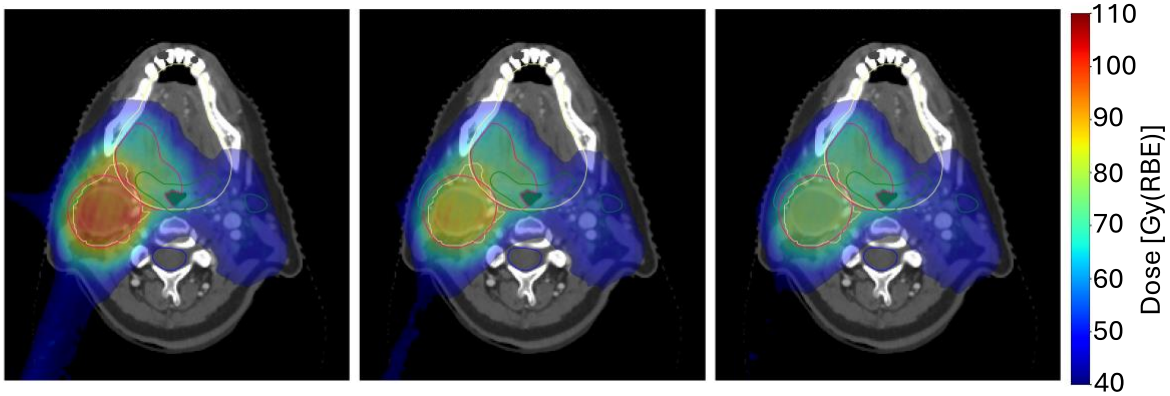

Figure 26: RBE-weighted dose distribution in one of the patients of the HNC patient cohort. The BTV, zCTV and relevant OARs are shown in the plots with colors as described in Table 11.

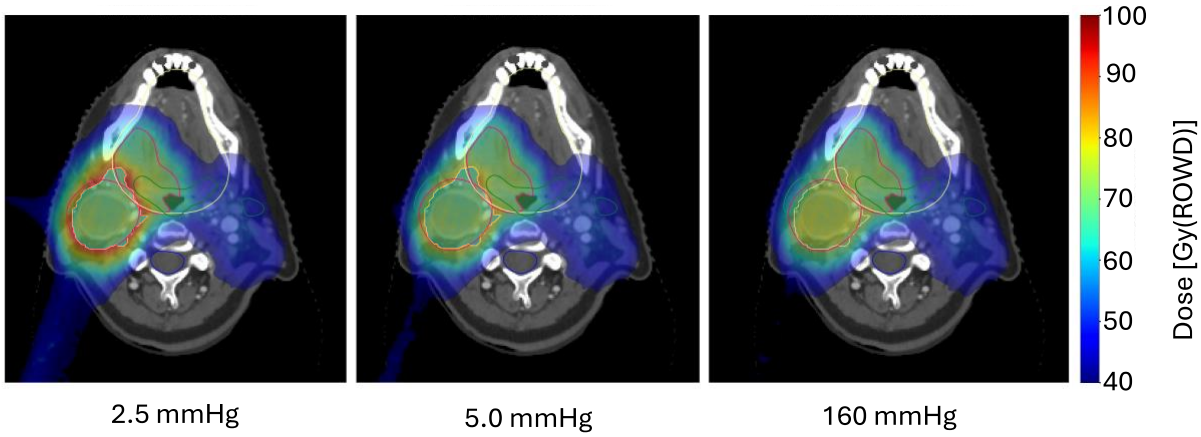

Figure 27: ROWD distribution in one of the patients of the HNC patient cohort. The BTV, zCTV and relevant OARs are shown in the plots with colors as described in Table 11.

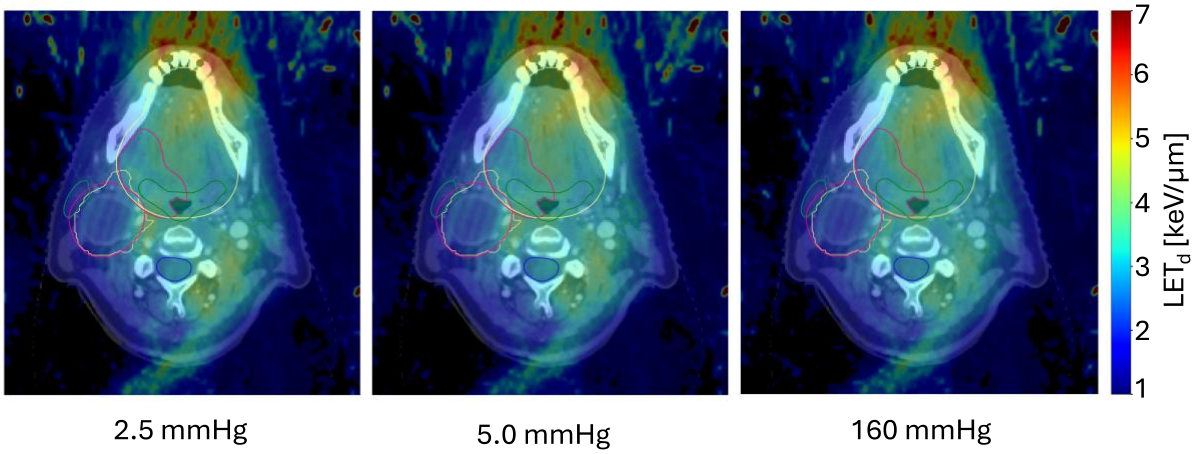

Figure 28: LET_d distribution in one of the patients of the HNC patient cohort. The BTV, zCTV and relevant OARs are shown in the plots with colors as described in Table 11.

7. Discussion

The motivation of this thesis was to determine the potential to increase the biological dose to the BTV through biological optimization using proton therapy in the most precise and effective way, and simultaneously spare the OARs, while testing and exploring the optimization tool. Different LET_d optimization strategies were explored on a water phantom, and ROWD optimization was performed on a water phantom and a HNC patient cohort. The optimizations were performed with an optimization tool developed at the University of Bergen. The feature of ROWD optimization was implemented in the optimization tool during the project.

7.1 Optimization parameters and objectives

As mentioned in section 5.4, different methods of defining the dose to the BTV were investigated in order to decide which method to use for dose objectives of the BTV for the rest of the simulations in the project. Method A, B and C, as defined in Table 3, were compared early in the project. Method A used the objective of mean dose of 2.2 Gy(RBE) to the BTV, method B used the objective of minimum dose of 2.2 Gy(RBE) to the BTV, while method C used the objectives of minimum dose of 2.2 Gy(RBE) and maximum dose of 2.4 Gy(RBE) to the BTV. The initial results favored method A, as the method resulted in a more homogeneous dose to the BTV compared to the other methods. The number of primaries per pencil beam of the MC simulation was later increased to achieve better statistics and more reliable results. This resulted in more similar results of the methods and similar homogeneity. Method A was still chosen as the way of defining the dose objective for the BTV.

As one of the project objectives was to test and explore the optimization software, several combinations of dose and LET_d objectives were tested in the project, as well as different weightings of the objectives. The chosen weightings of the objectives are a product of trying to achieve the prescribed dose and LET_d for all structures simultaneously.

The number of iterations in the optimizations was set to 100 for all simulations, but in several cases the cost function converged, and the optimization process did not complete all 100 iterations. The simulations of the water phantoms mostly finished all 100 iterations, while the patient plan simulations tended to converge before they reached 100 iterations. A possible reason for this could be that the optimization criteria were too strict or that they were conflicting. The patient plans had many more objectives than the water phantom, which could affect the convergence of the cost function. Although the optimization process did not complete all iterations, the optimization of the patient plans was still successful.

The RBE was set to 1.1 in this project. As the RBE is known to vary along the particle track, the results could be different if models of variable RBE were included. The DAH model of OER was used in the ROWD optimization. The aerobic pO_2 was set to 160 mmHg, which is common for *in vitro* studies. The DAH model originally uses an aerobic pO_2 of 30 mm, which is a considered a normoxic value in humans. This difference may have affected the ROWD slightly. As previously discussed, the normoxic pO_2 varies in different kinds of tissue, which complicates the work of achieving a correct OER and ROWD. The hypoxic pO_2 values of 2.5 mmHg and 5.0 mmHg are commonly used in research of hypoxic tumors, and was therefore used in this thesis [63, 64].

7.2 LET optimization of the water phantom

As shown in the DVH in Figure 13a) and the doses in Table 7, the difference in dose is relatively small when comparing the three optimization strategies. This applies for all the structures. This indicates that the optimization tool has the potential to include LET_d objectives without affecting the dose distributions significantly. As seen in Table 7, the median dose of the zCTV is 2.0 Gy(RBE) for all three optimization strategies, as prescribed. The median doses of the BTVs do however not reach the goal of 2.2 Gy(RBE) for any of the optimization strategies, despite the fact that the objectives of the BTVs had the highest weights. A reason for this might be that a higher dose to the BTV would increase the dose of the corresponding zCTV, as there is a physical

limitation of how steep the dose fall-off can be. Adjusting the weightings of the objectives might improve the dose delivery to the BTVs, but may simultaneously worsen the zCTV doses.

As most of the OAR doses were below the maximum constraint of 0.50 Gy(RBE) for all three optimization strategies, the results indicate that the maximum dose constraint of the OARs could be even lower. The position of the OAR with regards to the target volumes affect the dose of the OAR, and more complex geometries should be explored to investigate how well the optimization tool can reduce OAR dose. Nevertheless, the results show that the optimization tool has the potential for OAR sparing while simultaneously providing dose escalation to a tumor sub-volume.

The LVH in Figure 13b) shows a large increase of the LET_d in the BTVs when comparing the DE-LET_{BTV} and DE-$LET_{BTV,\ OAR}$ strategies with the DE strategy. When considering the LVH and DVH together, this shows the potential of the optimization tool to escalate the LET_d to a sub-volume, without affecting the corresponding dose significantly. The LET_d of the zCTV is also slightly elevated for the DE-LET_{BTV} and DE-$LET_{BTV,\ OAR}$ strategies, compared to the DE strategy. As seen in the color wash plots of LET_d distribution in Figure 15, the area of elevated LET_d in the BTVs extends to the zCTVs for the DE-LET_{BTV} and DE-$LET_{BTV,\ OAR}$ strategies. As none of the zCTVs have any LET_d objectives, this increase does not affect the cost function of the optimization process. As shown in the LVH and color wash plots of LET_d distribution, the LET_d of the OAR is significantly decreased for the DE-$LET_{BTV,\ OAR}$ strategy. This shows a potential of limiting high LET_d to OARs by using the optimization tool.

Adjusting the weight of the optimization objectives may lead to more a homogeneous dose and LET_d coverage of the BTV and the zCTV. A possible explanation to why including LET_d objectives in the optimization does not affect the dose in a large scale can be that the optimization is performed on a simple geometry with only one BTV and one OAR. The optimization tool should be tested on more complex geometries to determine the full potential of LET_d optimization with the optimization tool. Garrido-Hernandez et al. have performed LET optimization on a HNC patient cohort with the

optimization tool, which showed promising results regarding both dose escalation and LET escalation to a tumor sub-volume [65].

These results indicate that it is possible to increase the biological dose in the BTV, as well as sparing the OARs, by performing LET_d optimization together with dose escalation by using the optimization tool. The OAR dose was not increased significantly in of any of the optimization strategies that included a LET_d escalation of the BTV. The results also indicate that the LET_d of the OAR can be decreased at the same time as achieving an LET_d escalation in the BTV.

There are several other studies of LET optimization with IMPT on both water phantoms and various kinds of tumors [65-69]. Among the studies is a study by Cao et al., which performed LET_d optimization of IMPT plans of a brain tumor patient cohort, and achieved escalated LET in target volumes as well as decreased LET in OARs, without compromising the dose delivery [69]. An et al. performed "worst-case" robust optimization of IMPT plans of prostate cancer, lung cancer and HNC patients and compared conventional treatment plans to treatment plans with reduced LET in the OARs [67]. The results of these studies showed that LET can be reduced in OARs without decreasing the quality of dose coverage, which agree with the results of this thesis. No clinical studies of LET optimization with IMPT are published as of this date, but there are at least two ongoing clinical trials [70, 71].

7.3 ROWD optimization of the water phantom

As seen in the DVH in Figure 16a), all the BTVs are relatively homogeneous and reach the goals of prescribed ROWD, which indicates successful ROWD optimization with the optimization tool. The increase in RBE-weighted dose for the BTVs with pO_2 of 2.5 mmHg and 5.0 mmHg is seen in the DVH and is as expected and shows the potential of the optimization tool to escalate the RBE-weighted dose in a structure.

For the 2.5 mmHg BTV case it was observed that the optimization tool could not achieve a completely satisfactory ROWD for both the BTV and the zCTV at the same time. The weightings shown in Table 5 and Table 6 were chosen as they gave the most

satisfying results considering the ROWD distributions of the BTVs. In the color wash plots of RBE-weighted dose in Figure 26 one can observe a rim of elevated dose around the BTVs with pO_2 of 2.5 mmHg and 5.0 mmHg, which is largest around the BTV of pO_2 of 2.5 mmHg. The median doses are identical for all the zCTVs, but the $D_{2\%}$ increase with decreasing pO_2 of the corresponding BTV (Table 9). A reason for this is the rim of elevated dose around the BTV, as there are physical limitations of how steep a dose fall-off can be.

The LET_d of the BTV increases with decreasing pO_2, as seen in the LVH and color wash plots of LET_d distribution in Figure 16b) and Figure 19, respectively. The same trend was seen for the LET_d of the zCTV, which is increasing with decreasing pO_2 of the corresponding BTV. A reason for this might be the increased physical dose in the BTVs with pO_2 of 2.5 mmHg and 5.0 mmHg to account for the hypoxic effects, as well as the weightings of the pencil beams to achieve the elevated dose. More Bragg peaks will be situated in the BTV to provide a higher dose, and the LET is at its highest around the Bragg peak. As the LET is increasing with decreasing proton energy, the LET will be elevated in areas around the end of the beam. This is a possible explanation for the area of elevated LET_d in the zCTV around the BTV, as seen in the color wash plots of LET_d distribution (Figure 19).

Most of the OAR doses were below the maximum constraint of 0.50 Gy(ROWD), and the pO_2 of the corresponding BTVs did not affect the dose of the OARs significantly. This indicates that the objective of maximum dose to the OAR could be lowered. The position of the OAR compared to the BTV affects the dose delivered to the OAR, and more complicated geometries should be investigated to test the potential of ROWD optimization with the optimization tool. As the OARs corresponding to the BTVs with pO_2 of 2.5 mmHg and 5.0 mmHg had a lower $LET_{d,2\%}$ than the OAR corresponding to the DE BTV, there was no negative effect of ROWD optimization regarding the LET_d of the OARs. Further research is needed before this can be stated as a general trend. A possible reason for why the LET_d is higher in the OAR corresponding to the DE BTV compared to the OARs corresponding to the BTVs with pO_2 of 2.5 mmHg and 5.0

mmHg could be that the high LET_d is redirected to areas around the BTV for the latter cases when the physical dose is elevated.

The results indicate that the optimization tool has the potential to deliver the prescribed ROWD to a hypoxic sub-volume of the tumor, without affecting the dose of the OAR significantly.

7.4 ROWD optimization of HNC patient plans

The ROWD of the BTVs with pO_2 of 2.5 mmHg and 5.0 mmHg are homogeneous and achieve the goal of prescribed ROWD, which indicate successful ROWD optimization. The corresponding increase of RBE-weighted dose to account for hypoxia is large and shows that the optimization tool has the potential to escalate the dose to a high level for a smaller volume. This does however not mean that the RBE-weighted dose should be escalated to very high levels in clinical practice, as most patients are cured with the conventional treatment. A possible solution is 10 – 20 % dose escalation to the hypoxic BTVs.

As seen in the color wash plots of ROWD distribution in Figure 26, there is a rim of elevated dose around the BTVs with pO_2 of 2.5 mmHg and 5.0 mmHg that extends to the zCTVs. For some zCTVs the rim of elevated dose will take up more space relative to the total volume. This rim of elevated dose will affect the median dose and maximum dose of the zCTV compared to the CTVs that do not have a BTV on the inside. Possible reasons for the rim of elevated dose around the BTV are discussed in the previous section (7.3).

The mean median dose of the zCTVs is slightly higher than the prescribed 68 Gy(ROWD) in all cases (Figure 22), with a slight increase with decreasing pO_2 of the corresponding BTV. This might be due to the rim of high dose around the BTVs with pO_2 of 2.5 mmHg and 5.0 mmHg. The box plots of $D_{2\%}$ in Figure 23 show that the $D_{2\%}$ of the zCTVs increase with decreasing pO_2 of the corresponding BTV. The variation of $D_{2\%}$ of the zCTVs also increase with decreasing pO_2 of the corresponding BTV. A

reason for this might be the rim of high dose, as well the position of the zCTVs relative to the BTV and the rim of high dose.

As seen in the box plots of median LET_d and $LET_{d,2\%}$ in Figure 24 and Figure 25, respectively, there is no significant difference between the different levels of pO_2 of the corresponding BTV when considering the mean median LET_d and $LET_{d,2\%}$ of the zCTVs. Likewise, the LET_d of the BTVs does not differ noteworthy between the different values of pO_2, except for the BTV of one patient. There is no obvious reason for why the LET_d is increased with decreasing pO_2 in this case, and not for the other BTVs. The LET_d of the zCTVs and BTVs of the patient plans were in general not affected by the pO_2 of the BTVs, in contrast to the zCTVs and BTVs of the water phantom. The reason for this is not clear and should be further investigated by performing ROWD optimization on a wider range of patient plans.

As previously discussed, the dose restrictions of the OARs are based on the DAHANCA guidelines and [62]. As seen in the DVHs in Figure 20, there are in some cases great differences when comparing how much dose the OARs receive between the different patient plans. A reason for this is the different positions of target volumes relative to the OARs in the different patient plans. However, there is no general trend in increase or decrease of the doses and LET_d of the OARs for the different values of pO_2 of the corresponding BTVs. This indicates that it is possible to achieve a homogeneous ROWD to the BTV without affecting the OAR dose and LET_d noteworthy with the optimization tool. The metrics of dose and LET_d of the oral cavity was only available for 4 HNC patients, which resulted in less input data for the DVH, LVH and box plots for this structure. As no general trends were found for the OARs, this might not have affected the results.

No LET_d objectives were included in the ROWD optimization of the water phantom or the HNC patient cohort. As seen in the results of this project, the optimization tool is capable of dose escalation, ROWD optimization and LET_d optimization to a tumor sub-volume. Although not in the scope of this thesis, it would be interesting to perform LET_d optimization coupled with ROWD optimization to investigate if it is possible to

redirect high LET_d to the target volumes and decrease LET_d in the OARs as well as to simultaneously achieve a homogeneous ROWD in the target volumes.

There are some studies of ROWD optimization with IMPT, but the number of studies is limited [44, 72]. Henjum et al. performed voxel-by-voxel ROWD optimization on a HNC patient cohort [72]. Several RBE models were tested in the ROWD calculations. The study observed an increased RBE-weighted dose and LET to the hypoxic volumes while achieving the prescribed ROWD [72]. The increase of RBE-weighted dose corresponds with the results of this thesis. One cannot conclude that the results of Henjum et al. correspond with the results of this thesis regarding LET_d, as the results of how ROWD optimization affected the LET_d in the BTV varied between the ROWD optimization of the water phantom and the HNC patient cohort in this project [72].

Future work:

There are many interesting possibilities for future work regarding biological optimization with proton therapy. Future work may include further investigation of the capabilities of the optimization tool, for example by performing LET_d optimization on a broad range of patient treatment plans. Another possibility is to try to achieve a steeper dose fall-off with the optimization tool to reduce the dose to healthy tissue. ROWD optimization of hypoxic BTVs could be performed with different OER models to compare the differences between the models. Biologic optimizations with different RBE models could be compared to investigate the differences of a constant RBE model and variable RBE models.

Future work may also include ROWD optimization with a gradual pO_2 variation in the BTV structure, for example with decreasing pO_2 towards the center of the BTV. This would allow for a better simulation of gradual pO_2 variation in tumors and the ideal ROWD distribution. It would also be interesting to investigate ROWD optimization of hypoxic BTVs coupled with LET_d escalation to the BTV and LET_d restriction to OARs.

As the number of studies on LET optimization is increasing, there should be established guidelines of maximum LET_d to OARs as well as LET_d escalation goals for BTVs and

target volumes. Hence, there would be a unified standard of LET_d objectives that can be subject to further research.

8. Conclusion

Different strategies for optimization of biological dose to the BTV were developed and investigated with the optimization tool in this thesis. An IMPT plan was created for a water phantom, which was subsequently subjected to LET_d and ROWD optimization. The most promising ROWD optimization strategies were applied on a cohort of HNC patients. The LET_d optimization compared three optimization strategies, which included dose escalation and LET_d escalation to the BTV and LET_d restriction to the OAR. Strategies of ROWD optimization and dose escalation to assumed hypoxic BTVs were compared to investigate the effect of hypoxia and potential for a homogeneous ROWD in the target volumes with the optimization tool. The treatment plans were subject to FLUKA MC simulations and optimization with the optimization tool, developed at the University of Bergen. The feature of ROWD optimization was implemented in the optimization tool as a part of the project. The results of the LET_d optimization of the water phantom showed that the LET_d of the BTV could be escalated and the LET_d of the OAR decreased simultaneously, without affecting the dose of the structures significantly. The results of the ROWD optimization showed that it is possible to achieve a homogeneous ROWD to the relevant target volumes by using the optimization tool and indicate that ROWD optimization of tumor sub-volumes is possible with this approach. However, there is a challenge in knowing the exact pO_2 of the tumor, which create challenges for delivering the correct ROWD. There was no general trend of elevated dose to the OARs when comparing the ROWD optimizations strategies with different values of pO_2 of the corresponding BTV. The optimization of biological dose with the optimization tool was successful for both the LET_d and ROWD optimization. The results contribute to the idea of biological optimization being a promising technique in proton therapy which could significantly improve treatment as more precise techniques to quantify pO_2 emerge.

Bibliography

1. Strøm, M., et al., *Dødsårsaksregisteret. Dødsårsaker i Norge i 2022*. 2023, Folkehelseinstituttet: Oslo.
2. Norway, C.R.o., *Cancer in Norway 2019 - Cancer incidence, mortality, survival and prevalence in Norway*. 2020, Cancer Registry of Norway: Oslo.
3. Latoch, E., et al., *Late effects of childhood cancer treatment in long-term survivors diagnosed before the age of 3 years - A multicenter, nationwide study.* Cancer Epidemiol, 2022. **80**: p. 102209.
4. Ryder-Burbidge, C., et al., *The Burden of Late Effects and Related Risk Factors in Adolescent and Young Adult Cancer Survivors: A Scoping Review.* Cancers (Basel), 2021. **13**(19).
5. Hakansson, K., et al., *Radiation dose-painting with protons vs. photons for head-and-neck cancer.* Acta Oncol, 2020. **59**(5): p. 525-533.
6. Thorwarth, D., M. Soukup, and M. Alber, *Dose painting with IMPT, helical tomotherapy and IMXT: a dosimetric comparison.* Radiother Oncol, 2008. **86**(1): p. 30-4.
7. Wilson, R.R., *Radiological use of fast protons.* Radiology, 1946. **47**(5): p. 487-91.
8. Chang, D.S., et al., *Basic Radiotherapy Physics and Biology*. 2021, Springer Cham. p. XXIII, 380.
9. Flynn, R.T., et al., *Intensity-modulated x-ray (IMXT) versus proton (IMPT) therapy for theragnostic hypoxia-based dose painting.* Phys Med Biol, 2008. **53**(15): p. 4153-67.
10. Fleming, I.N., et al., *Imaging tumour hypoxia with positron emission tomography.* Br J Cancer, 2015. **112**(2): p. 238-50.
11. Bentzen, S.M. and V. Gregoire, *Molecular imaging-based dose painting: a novel paradigm for radiation therapy prescription.* Semin Radiat Oncol, 2011. **21**(2): p. 101-10.
12. Berman, A.T., S.S. James, and R. Rengan, *Proton Beam Therapy for Non-Small Cell Lung Cancer: Current Clinical Evidence and Future Directions.* Cancers (Basel), 2015. **7**(3): p. 1178-90.
13. Mohan, R. and D. Grosshans, *Proton therapy - Present and future.* Adv Drug Deliv Rev, 2017. **109**: p. 26-44.
14. Jones, B., *Why RBE must be a variable and not a constant in proton therapy.* Br J Radiol, 2016. **89**(1063): p. 20160116.
15. Paganetti, H., *Relative biological effectiveness (RBE) values for proton beam therapy. Variations as a function of biological endpoint, dose, and linear energy transfer.* Phys Med Biol, 2014. **59**(22): p. R419-72.
16. Shukla, A.K. and U. Kumar, *Positron emission tomography: An overview.* J Med Phys, 2006. **31**(1): p. 13-21.
17. Ling, C.C., et al., *Towards multidimensional radiotherapy (MD-CRT): biological imaging and biological conformality.* Int J Radiat Oncol Biol Phys, 2000. **47**(3): p. 551-60.
18. Garrido-Hernandez, G., et al., *Interim 18F-FDG-PET based response-adaptive dose escalation of proton therapy for head and neck cancer: a treatment planning feasibility study.* Submitted to Physica Medica.
19. Henjum, H., et al., *The Organ Sparing Potential of Different Biological Optimization Strategies in Proton Therapy.* Adv Radiat Oncol, 2021. **6**(6): p. 100776.

20. Mohan, R., et al., *Radiobiological issues in proton therapy.* Acta Oncol, 2017. **56**(11): p. 1367-1373.
21. Newhauser, W.D. and R. Zhang, *The physics of proton therapy.* Phys Med Biol, 2015. **60**(8): p. R155-209.
22. Guan, F., et al., *Analysis of the track- and dose-averaged LET and LET spectra in proton therapy using the geant4 Monte Carlo code.* Med Phys, 2015. **42**(11): p. 6234-47.
23. ICRU, *Report 85: Fundamental Quantities and Units for Ionizing Radiation.* Journal of the ICRU, 2011.
24. Vaupel, P., O. Thews, and M. Hoeckel, *Treatment resistance of solid tumors: role of hypoxia and anemia.* Med Oncol, 2001. **18**(4): p. 243-59.
25. Gray, L.H., et al., *The concentration of oxygen dissolved in tissues at the time of irradiation as a factor in radiotherapy.* Br J Radiol, 1953. **26**(312): p. 638-48.
26. Paganetti, H., et al., *Report of the AAPM TG-256 on the relative biological effectiveness of proton beams in radiation therapy.* Med Phys, 2019. **46**(3): p. e53-e78.
27. Paganetti, H., et al., *Relative biological effectiveness (RBE) values for proton beam therapy.* Int J Radiat Oncol Biol Phys, 2002. **53**(2): p. 407-21.
28. McNamara, A.L., J. Schuemann, and H. Paganetti, *A phenomenological relative biological effectiveness (RBE) model for proton therapy based on all published in vitro cell survival data.* Phys Med Biol, 2015. **60**(21): p. 8399-416.
29. Carabe-Fernandez, A., R.G. Dale, and B. Jones, *The incorporation of the concept of minimum RBE (RbEmin) into the linear-quadratic model and the potential for improved radiobiological analysis of high-LET treatments.* Int J Radiat Biol, 2007. **83**(1): p. 27-39.
30. Wedenberg, M., B.K. Lind, and B. Hardemark, *A model for the relative biological effectiveness of protons: the tissue specific parameter alpha/beta of photons is a predictor for the sensitivity to LET changes.* Acta Oncol, 2013. **52**(3): p. 580-8.
31. Wilkens, J.J. and U. Oelfke, *A phenomenological model for the relative biological effectiveness in therapeutic proton beams.* Phys Med Biol, 2004. **49**(13): p. 2811-25.
32. Lyngholm, E., et al., *An updated variable RBE model for proton therapy.* Phys Med Biol, 2024.
33. ICRU, *ICRU Report 78, Prescribing, Recording, and Reporting Proton-Beam Therapy.* Journal of the ICRU, 2007.
34. Unkelbach, J. and H. Paganetti, *Robust Proton Treatment Planning: Physical and Biological Optimization.* Semin Radiat Oncol, 2018. **28**(2): p. 88-96.
35. Bentzen, S.M., *Theragnostic imaging for radiation oncology: dose-painting by numbers.* Lancet Oncol, 2005. **6**(2): p. 112-7.
36. Burnet, N.G., et al., *Defining the tumour and target volumes for radiotherapy.* Cancer Imaging, 2004. **4**(2): p. 153-61.
37. ICRU, *Prescribing, Recording and Reporting Photon Beam Therapy. Report 50.* 1993, International Commission on Radiation Units and Measurements: Bethesda, MD.
38. ICRU, *Prescribing, Recording and Reporting Photon Beam Therapy (Supplement to ICRU Report 50). Report 62.* 1999, International Commission on Radiation Units and Measurements: Bethesda, MD.
39. Soto, D.E., et al., *Correlation between pretreatment FDG-PET biological target volume and anatomical location of failure after radiation therapy for head and neck cancers.* Radiother Oncol, 2008. **89**(1): p. 13-8.

40. Vaupel, P. and L. Harrison, *Tumor hypoxia: causative factors, compensatory mechanisms, and cellular response.* Oncologist, 2004. **9 Suppl 5**: p. 4-9.
41. Carreau, A., et al., *Why is the partial oxygen pressure of human tissues a crucial parameter? Small molecules and hypoxia.* J Cell Mol Med, 2011. **15**(6): p. 1239-53.
42. Silvoniemi, A., *Novel aspects for methodology and utilization of PET/CT imaging in head and neck cancer.* 2018.
43. Malinen, E., et al., *Adapting radiotherapy to hypoxic tumours.* Phys Med Biol, 2006. **51**(19): p. 4903-21.
44. Dahle, T.J., et al., *The FLUKA Monte Carlo code coupled with an OER model for biologically weighted dose calculations in proton therapy of hypoxic tumors.* Phys Med, 2020. **76**: p. 166-172.
45. Wenzl, T. and J.J. Wilkens, *Modelling of the oxygen enhancement ratio for ion beam radiation therapy.* Phys Med Biol, 2011. **56**(11): p. 3251-68.
46. Mein, S., et al., *Spot-Scanning Hadron Arc (SHArc) Therapy: A Study With Light and Heavy Ions.* Adv Radiat Oncol, 2021. **6**(3): p. 100661.
47. Strigari, L., et al., *Tumour control in ion beam radiotherapy with different ions in the presence of hypoxia: an oxygen enhancement ratio model based on the microdosimetric kinetic model.* Phys Med Biol, 2018. **63**(6): p. 065012.
48. Tinganelli, W., et al., *Kill-painting of hypoxic tumours in charged particle therapy.* Sci Rep, 2015. **5**: p. 17016.
49. Garrido-Hernandez, G., et al., *Hypoxia adapted relative biological effectiveness models for proton therapy: a simulation study.* Biomed Phys Eng Express, 2022. **8**(6).
50. Komar, G., et al., *18F-EF5: a new PET tracer for imaging hypoxia in head and neck cancer.* J Nucl Med, 2008. **49**(12): p. 1944-51.
51. Abdulla, S. *PET imaging*. 2021 10.10.2021; Available from: https://www.radiologycafe.com/frcr-physics-notes/molecular-imaging/pet-imaging/.
52. Harrison, R.L., *Introduction To Monte Carlo Simulation.* AIP Conf Proc, 2010. **1204**: p. 17-21.
53. Paganetti, H., *Proton Therapy Physics*, H. Paganetti, Editor. 2012, CRC Press: Boca Raton.
54. Jiang, H. and H. Paganetti, *Adaptation of GEANT4 to Monte Carlo dose calculations based on CT data.* Med Phys, 2004. **31**(10): p. 2811-8.
55. Battistoni, G., et al., *Overview of the FLUKA code.* Annals of Nuclear Energy, 2015. **82**: p. 10-18.
56. Böhlen, T.T., et al., *The FLUKA Code: Developments and Challenges for High Energy and Medical Applications.* Nuclear Data Sheets, 2014. **120**: p. 211-214.
57. Ferrari, A., et al., *FLUKA: a multi-particle transport code*. 2005: CERN-2005-10 (2005), INFN/TC_05/11, SLAC-R-773.
58. Vlachoudis, V., *FLAIR: A POWERFUL BUT USER FRIENDLY GRAPHICAL INTERFACE FOR FLUKA*, in *International Conference on Mathematics, Computational Methods & Reactor Physics (M&C 2009)*. 2009: Saratoga Springs, New York, USA.
59. Liu, W., et al., *Robust optimization of intensity modulated proton therapy.* Med Phys, 2012. **39**(2): p. 1079-91.
60. Beichel, R.R., et al., *Semiautomated segmentation of head and neck cancers in 18F-FDG PET scans: A just-enough-interaction approach.* Med Phys, 2016. **43**(6): p. 2948-2964.
61. Jensen, K., et al., *The Danish Head and Neck Cancer Group (DAHANCA) 2020 radiotherapy guidelines.* Radiother Oncol, 2020. **151**: p. 149-151.

62. Evensen, M.E., et al., *Mucosa-sparing dose painting of head and neck cancer.* Acta Oncol, 2022. **61**(2): p. 141-145.
63. Nordsmark, M., et al., *Prognostic value of tumor oxygenation in 397 head and neck tumors after primary radiation therapy. An international multi-center study.* Radiother Oncol, 2005. **77**(1): p. 18-24.
64. Stadler, P., et al., *Influence of the hypoxic subvolume on the survival of patients with head and neck cancer.* Int J Radiat Oncol Biol Phys, 1999. **44**(4): p. 749-54.
65. Garrido-Hernandez, G., et al., *Title.*
66. Feng, H., et al., *Per-voxel constraints to minimize hot spots in linear energy transfer-guided robust optimization for base of skull head and neck cancer patients in IMPT.* Med Phys, 2022. **49**(1): p. 632-647.
67. An, Y., et al., *Robust intensity-modulated proton therapy to reduce high linear energy transfer in organs at risk.* Med Phys, 2017. **44**(12): p. 6138-6147.
68. Liu, C., et al., *Robust Optimization for Intensity Modulated Proton Therapy to Redistribute High Linear Energy Transfer from Nearby Critical Organs to Tumors in Head and Neck Cancer.* Int J Radiat Oncol Biol Phys, 2020. **107**(1): p. 181-193.
69. Cao, W., et al., *Linear energy transfer incorporated intensity modulated proton therapy optimization.* Phys Med Biol, 2017. **63**(1): p. 015013.
70. ClinicalTrials.gov, *Identifier: NCT03750513. LET Optimized IMPT in Treating Pediatric Patients with Ependymoma*.
71. ClinicalTrials.gov, *Identifier: NCT03690921. LET-IMPT and Standard Chemotherapy in Treating Patients with Newly Diagnosed Stage I-III Anal Canal Squamous Cell Cancer*.
72. Henjum, H., et al., *Combined RBE and OER optimization in proton therapy with FLUKA based on EF5-PET.* J Appl Clin Med Phys, 2023. **24**(9): p. e14014.

Appendix A

```
2559        def biological_dose(self,x,i,rowd_index,robust_index =0):
2560                """Function that calculates biological dose for ROI #i with intensity x
2561                Must include different alpha beta values, TODO
2562
2563                    """
2564
2565                if robust_index ==0:
2566                        dose =  x.dot(self.sep_dose_list[i])
2567                else:
2568                        dose =x.dot(self.collected_dose_list[robust_index][i])
2569                #If we use an RBE of 1.1, we dont have to calculate a lot elsewise
2570                #if self.biological_model == "1.1":     #This is moved further down
2571                #       return dose*(1.1/OER),1.1
2572
2573                #Proton dose
2574
2575                #let_d[dose_np < float(self.let_co)] = 0
2576                #Define some arrays
2577                RBE_max =  np.zeros_like(self.sep_dose_list[i])
2578                RBE_min =  np.zeros_like(self.sep_dose_list[i])
2579                RBE =  np.zeros_like(self.sep_dose_list[i])
2580
2581                #Calculate LETd
2582                dose_p = x.dot(self.sep_dose_p_list[i])
2583                up = x.dot(self.sep_let_times_dosep[i])
2584                dose_p = sparse_to_numpy(dose_p)
2585                #print (dose)
2586                dose_np = sparse_to_numpy(dose)
2587                #print(dose_np)
2588                up = sparse_to_numpy(up)
2589                #down = np.dot(x, self.sep_dose_p_list[i])
2590                let_d = np.divide(up, dose_p)
2591
2592                #Because of we divide by zero (fix sometime), we need to convert the
2593                #infinity-values to zero
2594                let_d = np.nan_to_num(let_d)
2595
2596                if self.biological_model == "1.1":
2597                        if rowd_index == 0: # Do not calculate ROWD for structure
2598                                return dose*1.1,1.1
2599
2600                        else: # Calculate ROWD for structure
2601                                # ROWD calculation
2602                                #Constants for Dahle model for OER
2603                                a1 = 0.10 #Gy^-1
2604                                a2 = 0.0010 #micrometer/(Gy*keV)
2605                                a3 = 0.010 #Gy^-1
2606                                a4 = 0.0100 #micrometer/(Gy*keV)
2607                                b1 = 0.765 #Gy^-1
2608                                b2 = 0.273 #Gy^-1
2609                                p_a = 160 #mmHg, partial oxygen pressure in aerobic/normoxic condition
2610                                p_h = float(rowd) #mmHg, partial oxygen pressure in hypoxic condition
2611                                L = let_d #micrometer/keV, dose-averaged LET
2612                                K = 3 #mmHg
2613                                S = 0.1 #Survival fraction
2614
2615                                #Calculation of constants
2616                                alpha_a = ((a1 + a2*L)*p_a + (a3 + a4*L)*K) / (p_a + K) #alpha for aerobic/normoxic conditions
2617                                alpha_h = ((a1 + a2*L)*p_h + (a3 + a4*L)*K) / (p_h + K) #alpha for anaerobic/hypoxic conditions
2618                                beta_a = ((b1*p_a + b2*K) / (p_a + K))**2 #beta for aerobic/normoxic conditions
2619                                beta_h = ((b1*p_h + b2*K) / (p_h + K))**2 #beta for anaerobic/hypoxic conditions
2620
2621                                #OER calculation
2622                                OER = ((np.sqrt(alpha_h**2 - 4*beta_h*np.log(S)) - alpha_h) / (np.sqrt(alpha_a**2 - 4*beta_a*np.log(S)) - alpha_a)) * (beta_a / beta_h)
2623                                dose = sparse_to_numpy(dose)
2624
2625                                #If we use an RBE of 1.1, we dont have to calculate a lot elsewise
2626                                return sp.csr_matrix(dose*(1.1/OER)),1.1 #Returns ROWD
2627
```

Figure 29: Screenshot of a part of the code of the optimization tool. ROWD was implemented in several parts of the optimization tool, among them in the calculation of biological dose, as shown in the figure.

Appendix B

Usage-name (single "-")	Full-name (double "--")	Explanation	Default	What should be the input
its	iterations	Maximum number of iterations in the optimizer	20	Integer
its_upd	iterations_update	How often should the optimizer update plots and files	10	Integer
l	label	Name of the optimization. All files will be marked with this handel	None	String
-f	npzfile	Filename of the main file from the FLUKA simulation. This is a default value throughout and does probablye not need a change	scored_values.npz	String
opt_f	opt_param_file	Filename of the optimization parameters file.	opt_params.csv	String
let_co	let_cutoff	The dose value used for LET-cutoff. The LET in voxels with dose lower than this threshold will not be calculated	0.036	Float
ab	alpha_beta_ratio	The alpha beta ratio for the biological dose	3.76	Float
bio	bio_opt	Biological model used. As of now, only "1.1", and "MCN" is implemented	1.1	String
ro	robust_opt	Choose robust optimization model. "stochastic" and "minimax" are the two models implemented. An additional weighting of the main plan can also be added after the choosen model e.g "stochastic 2". If nothing is chosen, no robust optimization will be performed		String (+float)
para	parallell	Maximum number of cores in use for parallell optimization	4	Integer
ro_its	robust_iterations	Number of optimization iterations performed when using the minimax robust approach	3	Integer
dcm	dicom	Loaction of the DICOM files. Also, when chosen, creates DICOM-files for every chosen number of iterations. When not chosen, no DICOM will be produced		String
c_file	continue_file	File location ofa PB-file on which you want to continue from		String
single	plot_single	True/False. When chosen, plots every single iteration separately. If not, comparisson plots for every iteration will be made. This is recommended to include in the optimization	False	True when chosen
phys_dose	plot_physical_dose	True/False, includes the physical dose when chosen	False	True when chosen
frac	fractions	Number of fractions in the plan	1	Integer
g	gui	True/False, Activates the GUI, not ready atm		
eq_weight	equal_weighting	Instead of using the intensities, all weightings are set as equal.	False	True when chosen
norm	normalize	Normalizes the plan to a certain structure. The structure chosen is normalized so that the median dose is equal to the chosen normalization value. Write two values after this argumen: 1: the number of the structure you want to normalize to (same as in the optimization_parameters file), 2: The normalization value (total dose). These should be seperated by space e.g. "-norm 0 54" normalizes ROI number 0 to 54 Gy(RBE)		Int and float

Figure 30: Available optimization parameters of the optimization tool.